J. Fluid Mech. (1990), *vol.* 215, *pp.* 331–363
Printed in Great Britain

The deformation of a liquid drop moving normal to a plane wall

By C. POZRIKIDIS

Department of Applied Mechanics and Engineering Sciences, R-011, University of California, San Diego, La Jolla, CA 92122, USA

(Received 28 February 1989 and in revised form 17 October 1989)

The deformation of a viscous drop moving under the action of gravity normal to a plane solid wall is studied. Under the assumption of creeping flow, the motion is studied as a function of the viscosity ratio between the drop and the suspending fluid, of surface tension, and of the initial drop configuration. Using the boundary integral formulation, the flow inside and outside the drop is represented in terms of a combined distribution of a single-layer and a double-layer potential of Green functions over the drop surface. The densities of these distributions are identified with the discontinuity in the interfacial surface stress, and with the interfacial velocity. The problem is formulated as a Fredholm integral equation of the second kind for the interfacial velocity which is solved by successive iterations. It is found that in the absence of surface tension, a drop moving away from the wall obtains an increasingly prolate shape, eventually ejecting a trailing tail. Depending on the initial drop configuration, ambient fluid may be entrained into the drop along or away from the axis of motion. Surface tension prevents the formation of the tail allowing the drop to maintain a compact shape throughout its evolution. The deformation of the drop has little effect on its speed of rise. A drop moving towards the wall obtains an increasingly oblate shape. In the absence of surface tension, the drop starts spreading in the radial direction reducing into a thinning layer of fluid. This layer is susceptible to the gravitational Rayleigh–Taylor instability. Surface tension restricts spreading, and allows the drop to attain a nearly steady hydrostatic shape. This is quite insensitive to the viscosity ratio and to the initial drop configuration. The evolution of the thin layer of fluid which is trapped between the drop and the wall is examined in detail, and with reference to film-drainage theory. It is shown that the assumptions underlying this theory are accurate when the surface tension is sufficiently large, and when the viscosity of the drop is of the same or lower order of magnitude as the viscosity of the ambient fluid. The numerical results are discussed with reference to film-drainage asymptotic theories.

1. Introduction

The deformation of bubbles, drops, and cells moving under the action of gravity in an ambient suspending fluid has a long record in fluid dynamics research (Clift, Grace & Weber 1978). The problem has applications in diverse fields of science and engineering with characteristic examples the mechanics of emulsions, micro-mechanics of blood flow, microphysics of atmospheric precipitation, and convection in the Earth's mantle. The simplest possible configuration consists of a single drop moving at zero Reynolds number in an infinite ambient fluid. Early work by

Hadamard and Rybczynski (see Batchelor 1967) showed that such a drop may possess a perfectly spherical shape independently of surface tension. The stability of this shape was the subject of recent investigations by Kojima, Hinch & Acrivos (1984), Koh & Leal (1989), and Pozrikidis (1990). These studies showed that when not protected by surface tension, a non-spherical drop may suffer significant deformation. Depending on the initial shape, the drop may either develop a continuously elongating tail or transform into an almost-steady drop ring. These results acquire special significance by noting that in practice, a drop hardly ever moves in an infinite medium. The presence of fluid interfaces, solid boundaries, and other suspended particles introduce disturbances which cause the drop to deviate from the spherical configuration. It is then plausible that these disturbances initiate fluid motions which may lead to permanent deformation or even breakup. Understanding these motions requires further investigations.

A convenient prototype for analysing the interaction between a drop and a solid boundary is provided by the problem of a single drop moving towards or away from an infinite solid plane wall. Apart from its theoretical significance, this simple configuration has a direct relevance in a number of applications. For instance, drops moving away from a solid wall are encountered in heat and mass transfer processes that induce density variations or involve change of phase. Furthermore, spherical drops moving away from a solid boundary constitute popular models of cavity-type viscous plumes rising in the Earth's mantle (Whitehead 1988). The behaviour of a drop moving towards a solid wall emulates the close-range interaction between suspended drops and solid particles in systems of two-phase flow. Examples include filtration, and the flow of a dispersed liquid through a porous bed.

The problem of a drop moving towards or away from a plane wall has become the subject of several previous theoretical treatments. These may be cast into two general categories. One class of investigations consider the asymptotic limit of large surface tension, ensuring that the drop maintains a spherical or a nearly spherical shape throughout its evolution (Bart 1968; Chervenivanova & Zapryanov 1985, 1987). A second class of investigations consider the asymptotic behaviour of a drop settling on the wall, with primary focus on the evolution and breakup of the thin film which is trapped between the drop and the wall (Hartland 1967, 1969; Hartland & Robinson 1977; Dimitrov & Ivanov 1978; Jones & Wilson 1978; Wu & Weinbaum 1982; Lin & Slattery 1982; Chen 1984; Yiantsios & Davis 1990). It should be noted that the behaviour of this film is of considerable importance for it determines the overall shape of the drop as well as the time at which the drop adheres on the wall. This second class of studies consider the asymptotic limit of small Bond numbers $B = a^2|\Delta\rho|g/\gamma$ (where a is the equivalent drop radius, $\Delta\rho$ is the density difference between the drop and the suspending fluid, and γ is the surface tension) for which the deformation becomes important only when the drop is very close to the wall.

In this paper we undertake a numerical investigation of the deformation of a drop moving towards or away from a solid plane wall, relaxing the simplifying approximations adopted in previous studies. The two main assumptions of our analysis are that the drop moves normal to the wall, ensuring that the motion is axisymmetric, and that the flow occurs under conditions of creeping motion. Another assumption is that the interface between the drop and the suspending fluid is clean and thus it is characterized by constant surface tension. In our parametric investigations we seek to assess the effects of the viscosity ratio between the drop and the suspending fluid, of surface tension, and of the initial position and shape of the drop. Our strategy entails the numerical solution of a series of initial-value problems

in which a drop is released from a fixed location, and is free to rise or fall under the influence of gravity in a direction normal to the wall.

In the case of a drop moving towards the wall, one central goal of our investigation is to describe the birth and evolution of the film which is trapped between the settling drop and the wall. Experimental studies have shown that as a drop approaches a wall its lower surface flattens, eventually yielding an axisymmetric dimple. Despite persistent theoretical efforts, the exact mechanism of the formation and evolution of the dimple is not understood in a satisfactory manner. One of the problems of previous analyses is that they require information regarding the shape of the drop at an arbitrary initial instant, as well as the asymptotic shape of the drop beyond the rim of the dimple (Yiantsios & Davis 1990). In the asymptotic limit of small Bond numbers both of these shapes may be taken to be spherical, but in the more general case of moderate and large Bond numbers they are both determined by the history of drop deformation. The main objective of our investigation is then to shed light on the evolution of the trapped film under general flow conditions. Unfortunately, our numerical procedure is not able to produce high-accuracy results when surface tension is large or when the film is very thin, and thus it does not permit a direct comparison between our numerical results and previous asymptotic theories at small Bond numbers. Nevertheless, our results are able to validate the lubrication approximation, one of the central assumptions of the popular film-drainage theory.

To carry out our numerical investigations we develop a boundary integral formulation similar to that introduced by Rallison & Acrivos (1978) for unbounded flow. In our formulation we introduce two novel features. First, we develop a flow representation in terms of a compound distribution of single-layer and double-layer potentials. The densities of these potentials are proportional to the discontinuity in the surface stress across the fluid interface, and to the interfacial velocity. This representation differs from the classical boundary integral representation in which the density of the distributions is proportional to the surface stress and to the interfacial velocity. Our representation circumvents the need for solving an intermediate integral equation for the interfacial surface stress in order to construct the flow. By applying the boundary integral equation at the fluid interface we produce an integral equation for the interfacial velocity, similar to that derived by Rallison & Acrivos (1978). In our analysis, we show that this equation has a unique solution and a convergent resolvent for all finite values of the viscosity ratio between the drop and the suspending fluid. The second novel feature of our analysis is the numerical solution of the derived Fredholm integral equation of the second kind, by means of successive iterations. The advantages of this procedure include reduced cost of computations, high accuracy, and ease of implementation as discussed in a previous paper (Pozrikidis 1990).

In developing our boundary integral formulation, we take the opportunity to discuss certain properties of the Green function for Stokes flow bounded by a solid plane wall. Use of these Green functions in conjunction with boundary integral representations has been quite popular in elastostatics, but rather scarce in low-Reynolds-number hydrodynamics (see for instance Tran-Cong & Phan-Thien 1989). Using these Green functions allows a substantial reduction of the domain of the boundary integral representation. For the problem considered in this paper, the domain of the derived integral equation is reduced simply onto the drop surface.

In summary, the goal of this paper is to present a numerical investigation of the deformation of a drop moving towards a plane wall, viewed as a paradigm of deformation induced by the presence of a solid boundary. In §2 we present the

problem formulation and strategy of numerical solution. In §3 we present and discuss our numerical results, and in §4 we summarize our conclusions.

2. Analysis

2.1. *The Green function for flow bounded by a plane wall*

To prepare the ground for our analysis, we introduce the Green-function tensor $\boldsymbol{S}$ describing Stokes flow due to a point force in a domain bounded by a planar solid wall (Lorentz 1906, see Happel & Brenner 1986, p. 87). Thus, we state that

$$u_i(\boldsymbol{x}) = S_{ij}(\boldsymbol{x}, \boldsymbol{x}_0)\,\alpha_j \tag{2.1}$$

represents the velocity field due to a point force of strength $8\pi\alpha$ placed at the point $\boldsymbol{x}_0$, in the presence of a solid wall placed at $x = w$. By construction, $\boldsymbol{S}$ is required to vanish along the wall, that is

$$S_{ij}(\boldsymbol{x}, \boldsymbol{x}_0) = 0 \quad \text{when} \quad x = w. \tag{2.2}$$

Blake (1971) showed that $\boldsymbol{S}$ may be expressed in terms of a Stokeslet, and a finite collection of image singularities including an image Stokeslet, a potential dipole, and a Stokes-doublet:

$$\boldsymbol{S}(\boldsymbol{x}, \boldsymbol{x}_0) = \boldsymbol{S}^{\mathrm{ST}}(\hat{\boldsymbol{x}}) - \boldsymbol{S}^{\mathrm{ST}}(\tilde{\boldsymbol{x}}) + 2h^2\boldsymbol{S}^{\mathrm{D}}(\tilde{\boldsymbol{x}}) - 2h\boldsymbol{S}^{\mathrm{SD}}(\tilde{\boldsymbol{x}}), \tag{2.3}$$

where $h = x_0 - w$ is the distance of the point force from the wall, $\hat{\boldsymbol{x}} = \boldsymbol{x} - \boldsymbol{x}_0$, $\tilde{\boldsymbol{x}} = \boldsymbol{x} - \boldsymbol{x}_0^{\mathrm{IM}}$, and $\boldsymbol{x}_0^{\mathrm{IM}} = (2w - x_0, y_0, z_0)$ is the image of $\boldsymbol{x}_0$ with respect to the wall. The tensor $\boldsymbol{S}^{\mathrm{ST}}$ represents the free-space Stokeslet, whereas the tensors $\boldsymbol{S}^{\mathrm{D}}$ and $\boldsymbol{S}^{\mathrm{SD}}$ represent potential dipoles and Stokes doublets, and are defined as

$$S_{ij}^{\mathrm{ST}} = \frac{\delta_{ij}}{|\boldsymbol{x}|} + \frac{x_i x_j}{|\boldsymbol{x}|^3}, \quad S_{ij}^{\mathrm{D}} = \pm\frac{\partial}{\partial x_j}\left(\frac{x_i}{|\boldsymbol{x}|^3}\right), \quad S_{ij}^{\mathrm{SD}} = \pm\frac{\partial}{\partial x_j}(S_{il}^{\mathrm{ST}}) \tag{2.4a–c}$$

The plus sign corresponds to $j = 2, 3$ for the y- and z-axes, and a minus sign to $j = 1$ for the x-axis. In Appendix A we show that the tensor $\boldsymbol{S}$ satisfies the symmetry property

$$S_{ij}(\boldsymbol{x}, \boldsymbol{x}_0) = S_{ji}(\boldsymbol{x}_0, \boldsymbol{x}). \tag{2.5}$$

In fact, we show that this property is shared by all Green functions of the equations of creeping motion in domains that are bounded by any arbitrary solid surface.

The pressure and stress fields corresponding to the fundamental flow (2.1) may be written in terms of the pressure vector $\boldsymbol{p}$ and the stress tensor $\boldsymbol{T}$ as

$$P(\boldsymbol{x}) = \mu p_j(\boldsymbol{x}, \boldsymbol{x}_0)\,\alpha_j, \tag{2.6}$$

$$\sigma_{ik}(\boldsymbol{x}) = \mu T_{ijk}(\boldsymbol{x}, \boldsymbol{x}_0)\,\alpha_j. \tag{2.7}$$

By analogy with (2.3) we write

$$p_i(\boldsymbol{x}, \boldsymbol{x}_0) = p_i^{\mathrm{ST}}(\hat{\boldsymbol{x}}) - p_i^{\mathrm{ST}}(\tilde{\boldsymbol{x}}) - 2hp_i^{\mathrm{SD}}(\tilde{\boldsymbol{x}}) \tag{2.8}$$

and

$$\boldsymbol{T}(\boldsymbol{x}, \boldsymbol{x}_0) = \boldsymbol{T}^{\mathrm{ST}}(\hat{\boldsymbol{x}}) - \boldsymbol{T}^{\mathrm{ST}}(\tilde{\boldsymbol{x}}) + 2h^2\boldsymbol{T}^{\mathrm{D}}(\tilde{\boldsymbol{x}}) - 2h\boldsymbol{T}^{\mathrm{SD}}(\tilde{\boldsymbol{x}}), \tag{2.9}$$

where

$$p_i^{\mathrm{ST}} = 2\frac{x_i}{|\boldsymbol{x}|^3}, \quad T_{ijk}^{\mathrm{ST}}(\boldsymbol{x}) = -6\frac{x_i x_j x_k}{|\boldsymbol{x}|^5}, \tag{2.10a, b}$$

$$T_{ijk}^{\mathrm{D}}(\boldsymbol{x}) = \pm 6\left(-\frac{\delta_{ik}x_j + \delta_{ij}x_k + \delta_{kj}x_i}{|\boldsymbol{x}|^5} + 5\frac{x_i x_j x_k}{|\boldsymbol{x}|^7}\right), \tag{2.11}$$

$$p_i^{\mathrm{SD}} = \pm 2\frac{\partial}{\partial x_i}\left(\frac{x_1}{|\boldsymbol{x}|^3}\right), \quad T_{ijk}^{\mathrm{SD}}(\boldsymbol{x}) = x_1 T_{ijk}^{\mathrm{D}}(\boldsymbol{x}) \pm 6\left(\frac{\delta_{ik}x_j x_1 - \delta_{j1}x_i x_k}{|\boldsymbol{x}|^5}\right). \quad (2.12a, b)$$

All $\boldsymbol{S}$, $\boldsymbol{p}$, and $\boldsymbol{T}$ vanish when the Green function is placed right on the wall, that is when $x_0 = w$.

In Appendix A we show that the velocity fields

$$u_j(\boldsymbol{x}_0) = p_j(\boldsymbol{x}, \boldsymbol{x}_0)\,\beta \quad (2.13)$$

and

$$u_j(\boldsymbol{x}_0) = T_{ijk}(\boldsymbol{x}, \boldsymbol{x}_0)\,g_{ik}, \quad (2.14)$$

where β and $\boldsymbol{g}$ are constants, are legitimate singular solutions to the equations of creeping motion. Both of these velocity fields vanish along the wall at $x_0 = w$. Physically, (2.13) expresses the velocity field due to a point source of strength $-8\pi\beta$ located at the point $\boldsymbol{x}$, in the presence of the solid wall. For later use, we write the pressure field corresponding to the flow (2.14) in the symbolic form

$$P(\boldsymbol{x}_0) = \mu\Pi_{ij}(\boldsymbol{x}_0, \boldsymbol{x})\,g_{ij}. \quad (2.15)$$

The exact expression for the tensor $\boldsymbol{\Pi}$ is omitted in the interest of space.

2.2. *Integral representation*

We consider the motion of a viscous drop at vanishing Reynolds number in the vicinity of a solid planar wall, as illustrated in figure 1. We denote the drop with the subscript 2, and the ambient fluid with the subscript 1. Physical reasoning dictates that the velocity is continuous across the surface of the drop. The interfacial surface stress may undergo a discontinuity whose magnitude depends on the physical properties of the fluids, and on the physico-chemical characteristics of the fluid interface.

We begin our analysis by writing down the boundary integral equation for the flow external to the drop. Accounting for the fact that the flow vanishes at infinity, we obtain

$$u_j^{(1)}(\boldsymbol{x}_0) = -\frac{1}{8\pi\mu_1}\int_{\text{Drop and Wall}} f_i^{(1)}(\boldsymbol{x})\,S_{ij}(\boldsymbol{x}, \boldsymbol{x}_0)\,\mathrm{d}S(\boldsymbol{x}) + \frac{1}{8\pi}\int_{\text{Drop and Wall}} u_i(\boldsymbol{x})\,T_{ijk}(\boldsymbol{x}, \boldsymbol{x}_0)\,\hat{n}_k(\boldsymbol{x})\,\mathrm{d}S(\boldsymbol{x}). \quad (2.16)$$

In this equation $\boldsymbol{f}$ is the surface stress, $\boldsymbol{f} = \boldsymbol{\sigma}\cdot\hat{\boldsymbol{n}}$, where $\boldsymbol{\sigma}$ is the modified stress tensor defined with respect to the modified pressure $P_{\mathrm{mod}} = P - \rho\boldsymbol{g}\cdot\boldsymbol{x}$. The unit normal vector $\hat{\boldsymbol{n}}$ is directed towards the suspending fluid, as illustrated in figure 1. The kernels $\boldsymbol{S}$ and $\boldsymbol{T}$ are the Green functions for the velocity and the stress, and are given by (2.3) and (2.9). Because of (2.2), and of the requirement that $\boldsymbol{u}$ vanishes along the wall, the domain of integration in (2.16) may be reduced onto the drop surface. The symmetry property (2.5) then allows us to identify the single-layer potential on the right-hand side of (2.16) with the flow induced by an interfacial distribution of the Green functions of strength $\boldsymbol{f}$.

Next, we consider the test flow $S_{ij}(\boldsymbol{x}, \boldsymbol{x}_0)\,\alpha_j$ where the point $\boldsymbol{x}_0$ is located exterior to the drop, and α_j is an arbitrary constant. Applying the reciprocal theorem for this test flow and the internal flow $\boldsymbol{u}^{(2)}$ (Happel & Brenner 1986, §3–5), we obtain

$$\int_{\text{Drop}} f_i^{(2)}(\boldsymbol{x})\,S_{ij}(\boldsymbol{x}, \boldsymbol{x}_0)\,\mathrm{d}S(\boldsymbol{x}) - \mu_2\int_{\text{Drop}} u_i(\boldsymbol{x})\,T_{ijk}(\boldsymbol{x}, \boldsymbol{x}_0)\,\hat{n}_k(\boldsymbol{x})\,\mathrm{d}S(\boldsymbol{x}) = 0. \quad (2.17)$$

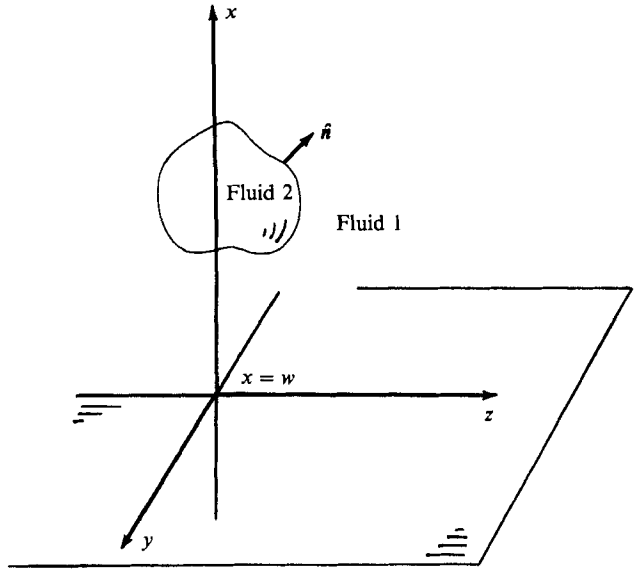

FIGURE 1. Schematic representation of a drop moving in the vicinity of a plane wall located at $x = w$.

Combining (2.16) and (2.17) yields

$$u_j^{(1)}(\boldsymbol{x}_0) = -\frac{1}{8\pi\mu_1}\int_{\text{Drop}} \Delta f_i(\boldsymbol{x})\, S_{ij}(\boldsymbol{x},\boldsymbol{x}_0)\,\mathrm{d}S(\boldsymbol{x}) + \frac{1-\lambda}{8\pi}\int_{\text{Drop}} u_i(\boldsymbol{x})\, T_{ijk}(\boldsymbol{x},\boldsymbol{x}_0)\,\hat{n}_k(\boldsymbol{x})\,\mathrm{d}S(\boldsymbol{x}), \tag{2.18}$$

where $\Delta\boldsymbol{f}$ is the jump in surface stress across the fluid interface equal to $\Delta\boldsymbol{f} = (\boldsymbol{\sigma}_1 - \boldsymbol{\sigma}_2)\cdot\hat{\boldsymbol{n}}$, and λ is the viscosity ratio $\lambda = \mu_2/\mu_1$. Effectively, we have managed to express the external flow as a combined distribution of single-layer and double-layer potentials. The densities of these potentials are proportional to the discontinuity in the interfacial surface stress, and to the interfacial velocity. The pressure field corresponding to (2.18) is given by

$$P^{(1)}(\boldsymbol{x}_0) = -\frac{1}{8\pi\mu_1}\int_{\text{Drop}} p_i(\boldsymbol{x}_0,\boldsymbol{x})\,\Delta f_i(\boldsymbol{x})\,\mathrm{d}S(\boldsymbol{x}) + \frac{1-\lambda}{8\pi}\int_{\text{Drop}} \Pi_{ik}(\boldsymbol{x}_0,\boldsymbol{x})\, u_i(\boldsymbol{x})\,\hat{n}_k(\boldsymbol{x})\,\mathrm{d}S(\boldsymbol{x}), \tag{2.19}$$

where $\boldsymbol{p}$ and $\boldsymbol{\Pi}$ were given by (2.8) and (2.15).

Repeating the above procedure for the internal flow we derive an integral representation for the internal flow:

$$u_j^{(2)}(\boldsymbol{x}_0) = -\frac{1}{8\pi\mu_1\lambda}\int_{\text{Drop}} \Delta f_i(\boldsymbol{x})\, S_{ij}(\boldsymbol{x},\boldsymbol{x}_0)\,\mathrm{d}S(\boldsymbol{x}) + \frac{1}{8\pi}\frac{1-\lambda}{\lambda}\int_{\text{Drop}} u_i(\boldsymbol{x})\, T_{ijk}(\boldsymbol{x},\boldsymbol{x}_0)\,\hat{n}_k(\boldsymbol{x})\,\mathrm{d}S(\boldsymbol{x}) \tag{2.20}$$

(Pozrikidis 1990). Note that this is identical to (2.18), except that the right-hand side

is divided by the viscosity ratio λ. The pressure field corresponding to (2.20) is given by (2.19), except that the right-hand side is divided by λ.

As a final step, we consider the limiting behaviour of (2.18) and (2.20), as the point $\boldsymbol{x}_0$ approaches the boundary of the drop from either side. The double-layer integrals in these equations may be written in terms of their Cauchy principal value as

$$\int_{\text{Drop}} u_i(\boldsymbol{x})\, T_{ijk}(\boldsymbol{x}, \boldsymbol{x}_0)\, \hat{n}_k(\boldsymbol{x})\, \mathrm{d}S(\boldsymbol{x}) = \pm 4\pi\, u_i(\boldsymbol{x}_0) + \int_{\text{Drop}}^{\text{PVI}} u_i(\boldsymbol{x})\, T_{ijk}(\boldsymbol{x}, \boldsymbol{x}_0)\, \hat{n}_k(\boldsymbol{x})\, \mathrm{d}S(\boldsymbol{x}), \quad (2.21)$$

where the plus sign is for the external side, the minus sign is for the internal side, and PVI stands for the Principal Value Integral. Substituting (2.21) into (2.18) or (2.20), we obtain the equation

$$u_j(\boldsymbol{x}_0) = -\frac{1}{4\pi\mu_1}\frac{1}{\lambda+1}\int_{\text{Drop}} \Delta f_i(\boldsymbol{x})\, S_{ij}(\boldsymbol{x}, \boldsymbol{x}_0)\, \mathrm{d}S(\boldsymbol{x}) + \frac{\beta}{4\pi}\int_{\text{Drop}}^{\text{PVI}} u_i(\boldsymbol{x})\, T_{ijk}(\boldsymbol{x}, \boldsymbol{x}_0)\, \hat{n}_k(\boldsymbol{x})\, \mathrm{d}S(\boldsymbol{x}), \quad (2.22)$$

where $\beta = (1-\lambda)/(1+\lambda)$. Specifying $\Delta \boldsymbol{f}$ renders (2.22) a Fredholm integral equation of the second kind for the interfacial velocity $\boldsymbol{u}$. This is similar in nature to the equation developed by Rallison & Acrivos (1978) for unbounded flow. In the case of a drop moving under the influence of gravitational and capillary forces we have

$$\Delta \boldsymbol{f} = [\Delta\rho g x + \gamma \nabla \cdot \hat{\boldsymbol{n}}]\, \hat{\boldsymbol{n}}, \quad (2.23)$$

where γ is the surface tension of the interface (assumed to be isotropic and uniform), $\Delta\rho = \rho_2 - \rho_1$, and the gravity vector points towards the negative x-axis.

To assess the uniqueness of solution of the integral equation (2.22), but also to investigate the feasibility of an iterative procedure of solution, we consider the corresponding homogeneous equation and inquire whether it possesses any real or complex eigenvalues β. Following an analysis similar to that presented by Pozrikidis (1990) for unbounded flow, we find that (2.22) has only real eigenvalues with magnitude greater or equal to one; $\beta = \pm 1$ are two eigenvalues corresponding to $\lambda \neq 0, \infty$, with one and six eigensolutions respectively. Details of the analysis are omitted in the interest of space. These results guarantee that (2.22) has a unique solution, and that it can be successfully solved in an iterative manner for any finite value of the viscosity ratio λ.

Having solving the integral equation (2.22) for the interfacial velocity, we may compute the velocity field outside the drop using either one of the integral representations (2.16) or (2.18) (similar equations apply for the internal flow). Using the first representation requires knowledge of the boundary velocity as well as of the boundary surface stress $\boldsymbol{f}$ on either side of the fluid interface. The former is known, and the latter may be computed by applying (2.16) at the interface, and then, by solving the resulting Fredholm integral equation of the first kind for $\boldsymbol{f}$ (Stone & Leal 1989; Chi & Leal 1989; Ascoli, Dandy & Leal 1990). In contrast, using the representation (2.18) permits the computation of the velocity field directly from the calculated interfacial velocity, and from the known discontinuity in interfacial surface stress. Thus, it offers increased accuracy and significant savings in the cost of the computations, and for these reasons, it is adopted in our computations.

2.3. *Procedure of numerical solution*

For convenience, we rewrite (2.22) in the symbolic form

$$u_j = -\frac{1}{4\pi\mu_1}\frac{1}{\lambda+1}A_j + \frac{\beta}{4\pi}B_j \tag{2.24}$$

where $\boldsymbol{A}$ and $\boldsymbol{B}$ represent the single-layer and double-layer potential respectively. Both $\boldsymbol{A}$ and $\boldsymbol{B}$ are singular, and their accurate evaluation requires special attention. To remove the singularity of the double-layer potential, we use the identities

$$\int_{\text{Drop}}^{\text{PVI}} T^{\text{ST}}_{ijk}(\boldsymbol{x}, \boldsymbol{x}_0)\, \hat{n}_k(\boldsymbol{x})\, \mathrm{d}S(\boldsymbol{x}) = -4\pi\, \delta_{ij}, \tag{2.25a}$$

$$\int_{\text{Drop}}^{\text{PVI}} T_{ijk}(\boldsymbol{x}, \boldsymbol{x}_0)\, \hat{n}_k(\boldsymbol{x})\, \mathrm{d}S(\boldsymbol{x}) = -4\pi\, \delta_{ij}, \tag{2.25b}$$

where $\boldsymbol{T}^{\text{ST}}$ and $\boldsymbol{T}$ are the stress tensor of the free-space Stokeslet and of the Green function respectively. These allow us to write

$$B_j(\boldsymbol{x}_0) \equiv \int_{\text{Drop}}^{\text{PVI}} u_i(\boldsymbol{x})\, T_{ijk}(\boldsymbol{x}, \boldsymbol{x}_0)\, \hat{n}_k(\boldsymbol{x})\, \mathrm{d}S(\boldsymbol{x}) \equiv C_j(\boldsymbol{x}_0) - 4\pi\, u_j(\boldsymbol{x}_0), \tag{2.26}$$

where

$$C_j(\boldsymbol{x}_0) = \int_{\text{Drop}} [u_1(\boldsymbol{x}) - u_1(\boldsymbol{x}_0)]\, T_{1jk}(\boldsymbol{x}, \boldsymbol{x}_0)\, \hat{n}_k(\boldsymbol{x})\, \mathrm{d}S(\boldsymbol{x}) + \int_{\text{Drop}} [u_m(\boldsymbol{x})\, T_{mjk}(\boldsymbol{x}, \boldsymbol{x}_0) - u_m(\boldsymbol{x}_0)\, T^{\text{ST}}_{mjk}(\boldsymbol{x}, \boldsymbol{x}_0)]\, \hat{n}_k(\boldsymbol{x})\, \mathrm{d}S(\boldsymbol{x}), \tag{2.27}$$

and $m = 2, 3$. The two integrals in (2.27) are regular and may be computed using a standard integration procedure. It should be noted that the above choice of desingularization facilitates the computation of the integrals in the case of axisymmetric motion.

Exploiting the assumption of axisymmetry, we now perform all integrations in the azimuthal direction, reducing the surface integrals into line integrals over the drop contour in a meridian plane. Referring to cylindrical polar coordinates, we find for the single-layer potential

$$A_\alpha(\boldsymbol{x}_0) = -\int_C (x + \Gamma\nabla\cdot\hat{\boldsymbol{n}})\, M_{\alpha\beta}(\boldsymbol{x}, \boldsymbol{x}_0)\, \hat{n}_\beta(\boldsymbol{x})\, \mathrm{d}l(\boldsymbol{x}) \tag{2.28}$$

and for the double-layer potential

$$B_\alpha(\boldsymbol{x}_0) \equiv C_\alpha(\boldsymbol{x}_0) - 4\pi\, u_\alpha(\boldsymbol{x}_0), \tag{2.29a}$$

$$C_\alpha(\boldsymbol{x}_0) = \int_S \{[u_1(\boldsymbol{x}) - u_1(\boldsymbol{x}_0)]\, q_{\alpha 1\beta}(\boldsymbol{x}, \boldsymbol{x}_0) + u_2(\boldsymbol{x})\, q_{\alpha 2\beta}(\boldsymbol{x}, \boldsymbol{x}_0)\}\, \hat{n}_\beta(\boldsymbol{x})\, \mathrm{d}l(\boldsymbol{x}) - u_2(\boldsymbol{x}_0) \int_S p_{\alpha\beta}(\boldsymbol{x}, \boldsymbol{x}_0)\, \hat{n}_\beta(\boldsymbol{x})\, \mathrm{d}l(\boldsymbol{x}) \tag{2.29b}$$

where Greek indices take the values 1 and 2 for the x- and the σ-direction respectively. The matrices $\boldsymbol{M}$, $\boldsymbol{q}$, and $\boldsymbol{p}$ are given in Appendix B in a form suitable for computer implementation.

Our numerical procedure for solving the integral equation (2.24) is similar to that developed by Pozrikidis (1990). Briefly, this entails representation of the drop contour using a set of marker points, and discretization of the drop boundary into a set of circular arcs defined by three successive marker points. As $\boldsymbol{x} \to \boldsymbol{x}_0$, the single-layer potential (2.28) presents a logarithmic singularity which we subtract-off and integrate analytically over a circular arc. We compute all regular integrals using the six-point Gauss–Legendre quadrature over each arc. Finally, we solve the integral equation (2.24) by successive iterations, that is by guessing an initial interfacial velocity distribution, computing the right-hand side of the integral equation, and then, replacing the initial with the newly computed distribution. The iterations terminate when all components of two successive iterants differ by an amount which is less than a specified minimum. The success of this procedure hinges upon the fact that (2.22) has a convergent Neumann series, as guaranteed by the lack of real or complex eigenvalues of the corresponding homogeneous equation. Having computed the interfacial velocity, we advance the position of the marker points using the modified Euler's method. An essential component of the numerical procedure is the use of an adaptive point redistribution technique that allows us to pursue the development of regions of high curvature while maintaining the number of points at a moderate level. Details of this technique are given by Pozrikidis (1990). For moderate drop deformations, 24 to 32 points along the drop contour were typically used. For large deformations, a typical calculation started with 24 points and ended with 70 points. At high values of the surface tension, numerical instabilities set in requiring a proportional decrease in the size of the time step and an exceedingly large amount of computational time (see Pozrikidis 1990). These instabilities placed limits in the parametric space of our investigations.

To monitor the accuracy of the calculations, after each time step we computed the drop volume. For vanishing surface tension, the maximum change this volume was always less than 1.00%. For finite surface tension, the change in volume was more pronounced, and in extreme cases, it escalated up to 2%. Furthermore, to ensure that the computed drop shapes were accurate to plotting line width, we carried out a number of test computations varying the number of points and the size of the time step. We also performed favourable comparisons with available analytical solutions, as discussed in the next section. All computations were performed on the CRAY/XM-P computer of the San Diego Supercomputer Center. A complete run consumed approximately 45 min of CPU time.

3. Results and discussion

We consider the axisymmetric deformation of a viscous drop moving towards or away from an infinite solid wall. We reduce all flow variables using as characteristic lengthscale the equivalent drop radius a, and as characteristic timescale $\mu_1/ag|\Delta\rho|$, where $\Delta\rho = \rho_2 - \rho_1$. The evolution of the drop is a function of the initial shape of the drop, the initial distance from the wall, and of two physical parameters: the viscosity ratio $\lambda = \mu_2/\mu_1$, and the inverse Bond number $\Gamma = \gamma/a^2|\Delta\rho|g$. To reduce the dimensionality of our parametric investigation, we consider drops having an initial shape of a prolate or oblate spheroid with their axis normal to the wall. More specifically, we stipulate that at the initial instant, the distance between the centre of the drop and the wall is equal to δ, and the shape of the drop is described by

$$r = \alpha(1 + \epsilon P_2(\cos\theta)), \tag{3.1}$$

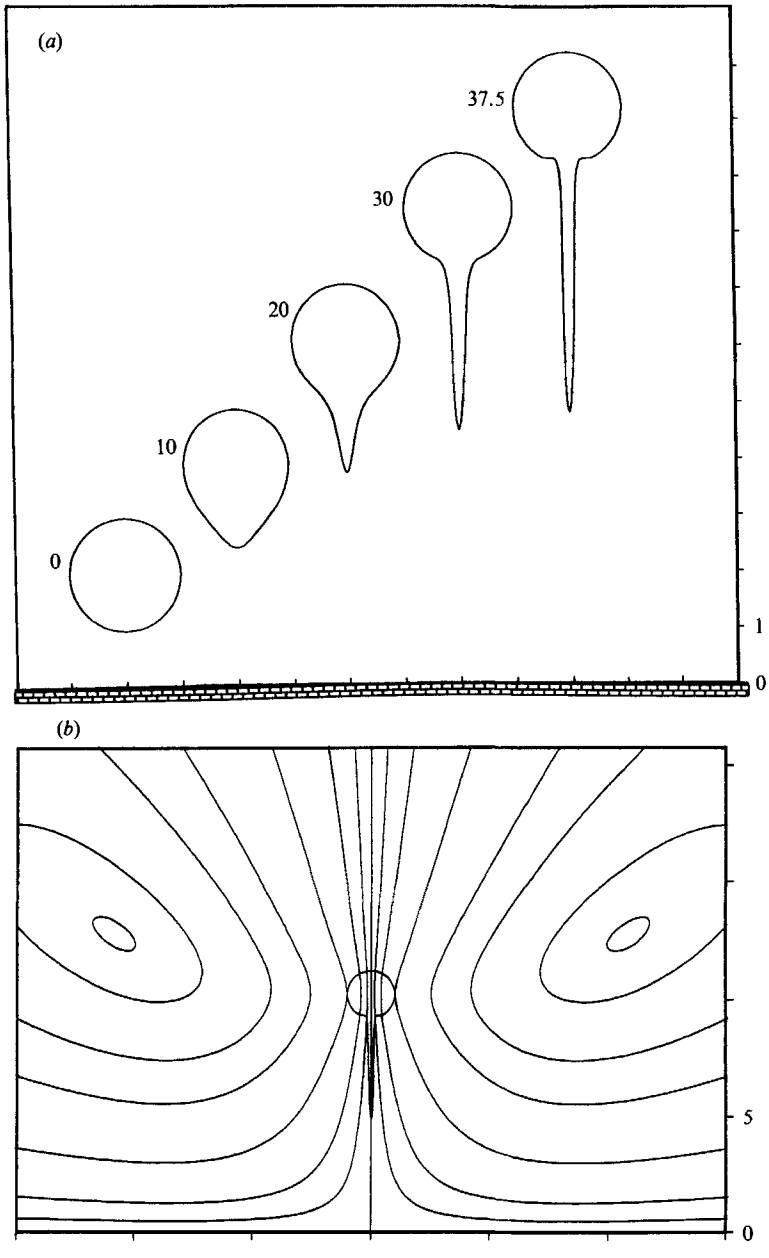

FIGURE 2. (a) Successive stages in the evolution of an initially spherical drop rising away from a plane wall, for $\lambda = 1$, $\Gamma = 0$, $\delta = 2.0$. The time is indicated on the left of each frame. (b) Streamline pattern at $t = 37.50$.

where P_2 is a Legendre polynomial. The value of α is chosen such that the dimensionless volume of the drop is equal to $\frac{4}{3}\pi$. The evolution of the drop is a function of the four parameters ϵ, δ, λ, Γ, and of the direction of motion.

3.1. *Drops moving away from the wall*

First, we consider drops moving away from the wall. In figure 2(a) we present characteristic stages in the evolution of a spherical drop, initially located at $\delta = 2$,

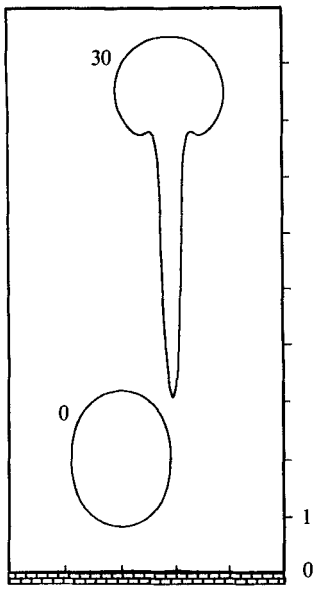

FIGURE 3

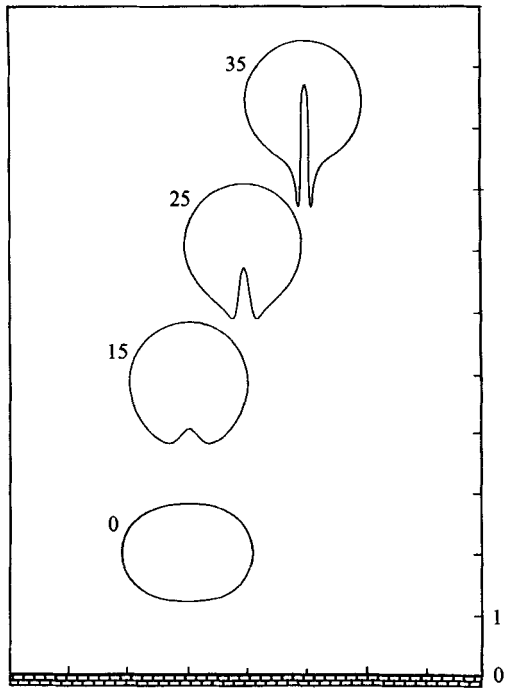

FIGURE 4

FIGURE 3. Two stages in the evolution of an initially prolate drop with $\epsilon = 0.20$, rising away from a plane wall, for $\lambda = 1$, $\Gamma = 0$, $\delta = 2.0$. The time is indicated on the left of each frame.

FIGURE 4. Successive stages in the evolution of an initially oblate drop with $\epsilon = -0.20$, rising away from a plane wall, for $\lambda = 1$, $\Gamma = 0$, $\delta = 2.0$. The time is indicated on the left of each frame.

with $\lambda = 1$ and vanishing surface tension $\Gamma = 0$. In the initial stages of deformation the drop obtains a spindle-like shape with a nearly spherical front and a conical back. The bottom part of the drop undergoes continuous elongation partly due to its self-induced motion, and partly due to extensional flow associated with the presence of the wall. As time progresses, a certain amount of fluid escapes from the drop to form an elongating tail, while the main body of the drop tends to recover the spherical shape. As the drop moves away from the wall, the flow due to the presence of the wall becomes of decreasing importance, and the evolution of the drop becomes very similar to that of a prolate drop rising in an infinite fluid. The slight indentation of the drop contour near the base of the tail, shown in figure 2(*a*) at $t = 37.50$, suggests that at large times, a thin filament of ambient fluid will enter the drop near the base of the tail. Asymptotically, at large times, the drop is expected to obtain a composite shape consisting of (i) an almost-spherical main body that contains a spiralling thin filament of entrained ambient fluid, and (ii) a continuously elongating tail (Pozrikidis 1990). To visualize the flow field generated by the motion of the drop, in figure 2(*b*) we present the instantaneous streamline pattern at $t = 37.50$. The most notable feature of this pattern is a family of closed streamlines composing a viscous eddy. The axial and radial positions of the centre of this eddy are approximately equal to the axial distance of the centre of the drop from the wall. Far away from the drop, the flow field resembles that induced by a ring of Stokeslets oriented in the axial direction (Liron & Blake 1981, §3).

To illustrate the effect of the initial shape of the drop, in figures 3 and 4 we present

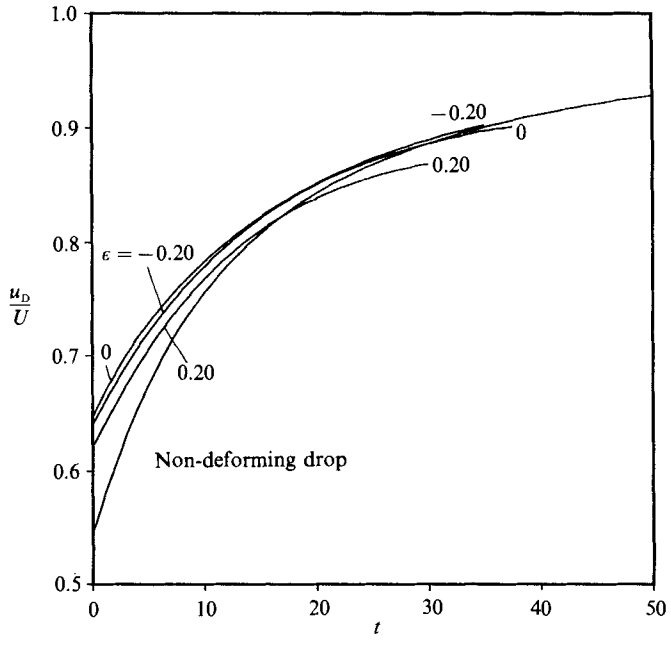

FIGURE 5. The vertical speed of the top of the drop u_D, reduced by the terminal velocity of the drop U, as a function of time, for $\lambda = 1$, $\Gamma = 0$, $\delta = 2.0$. The curve for the spherical non-deforming drop was derived from the theory of Bart (1968).

characteristic stages during the evolution of two initially spheroidal drops with $\epsilon = 0.20$ and -0.20, and for $\delta = 2$, $\lambda = 1$, and $\Gamma = 0$. The evolution of the prolate drop, shown in figure 3, is qualitatively similar to that of the spherical drop shown in figure 2(*a*). A comparison between figures 2(*a*) and 3 indicates that increasing the initial eccentricity of the drop increases the amount of drop fluid that escapes into the tail. This behaviour is similar to that of prolate drops evolving in an infinite ambient fluid (Pozrikidis 1990). The evolution of the oblate drop, shown in figure 4, presents certain novel features. To interpret these features, it is helpful to keep in mind that the image flow due to the presence of the wall tends to elongate the drop in the axial direction, causing it to obtain a prolate shape. In contrast, the self-induced motion of the drop associated with the oblate shape tends to elongate in the radial direction, causing it to obtain an increasingly more oblate shape (Pozrikidis 1990). Figure 4 suggests that these two counteracting mechanisms do not cancel each other but, instead, they work in a synergistic fashion. The net result, is the formation of a hollow dimple at the bottom of the drop. Ambient fluid is entrained into the drop along the centre of the dimple, and is convected towards the front of the drop transforming the drop into a ring. The lips of the dimple are extended by the local stagnation-point flow producing a thin axisymmetric filament of drop fluid.

Having presented three characteristic scenarios of evolution, we now consider how the deformation of the drop affects its speed of rise. In figure 5 we plot the axial velocity of the top of the drop as a function of time for the three cases depicted in figures 2(*a*), 3, and 4. In this figure we have also included the theoretical curve of Bart (1968) for a non-deforming spherical drop (see also Appendix C). We observe that at small times, the speed of the deforming spherical drop, $\epsilon = 0$, is higher than that of either the oblate or the prolate drop, $\epsilon = 0.20, -0.20$. This may be attributed to the reduced drag associated with the minimal surface area of the spherical shape.

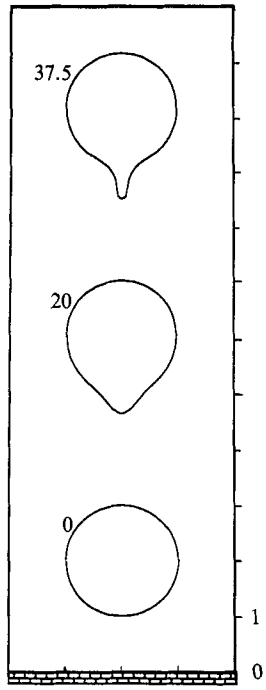

FIGURE 6. Three stages in the evolution of an initially spherical drop rising away from a plane wall, for $\lambda = 1$, $\Gamma = 0.10$, $\delta = 2.0$. The time is indicated on the left of each frame.

At large times, the prolate drop rises at a notably slower rate than either the spherical or the oblate drop. This is attributed to the reduced volume of the main body of this drop, as well as to the increased surface area of the developing tail. The oblate drop rises faster than the spherical or the prolate drop. This may be attributed to the compact shape maintained by this drop throughout its evolution. Comparing now our numerical results with the theoretical predictions of Bart, we find that at the initial stages of the motion, a deforming drop rises faster than a non-deforming drop. This suggests that the increase in drag due to the increasing surface area of the deforming drop is overcompensated by the decrease in drag due to the drop deformability. At large times, the numerical and theoretical curves show good agreement. Overall, we may conclude that the theory of non-deforming drops provides a reasonable estimate for the speed of rise of deforming drops, and may be used safely in engineering design.

Proceeding with our parametric investigation, we consider the effect of surface tension while maintaining the viscosity ratio at the convenient value $\lambda = 1$. We thus direct our attention to an initially spherical drop located at $\delta = 2$, and examine the evolution as a function of the inverse Bond number Γ. In figure 6 we show typical evolution stages for $\Gamma = 0.10$. It is clear that finite surface tension stabilizes the drop against the deforming action of the wall. This value of Γ is not large enough to suppress the formation of a tail, although it is capable of drastically reducing the size of the tail. It is also clear that finite surface tension prevents drop filamentation. Increasing Γ to 0.50 stabilizes the drop, allowing it to maintain its compact shape throughout its motion. The effect of surface tension on the speed of rise of the drop is illustrated in figure 7. The curve labelled $\Gamma = \infty$ is based on the assumption of a perfectly spherical shape, and was derived from the theory of Bart (1968). It is

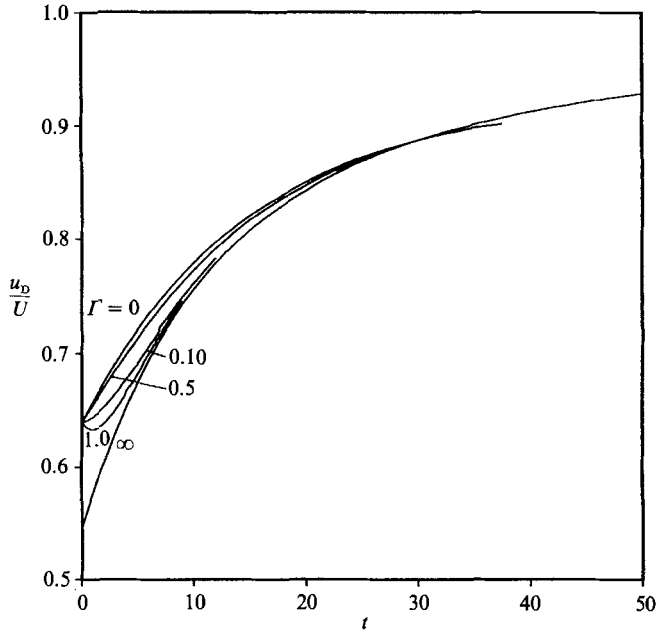

FIGURE 7. The vertical speed of the front of the drop u_D, reduced by the terminal drop velocity U, as a function of time, for $\lambda = 1$, $\epsilon = 0$, $\delta = 2.0$. The curve labelled ∞ was derived from the theory of Bart (1968).

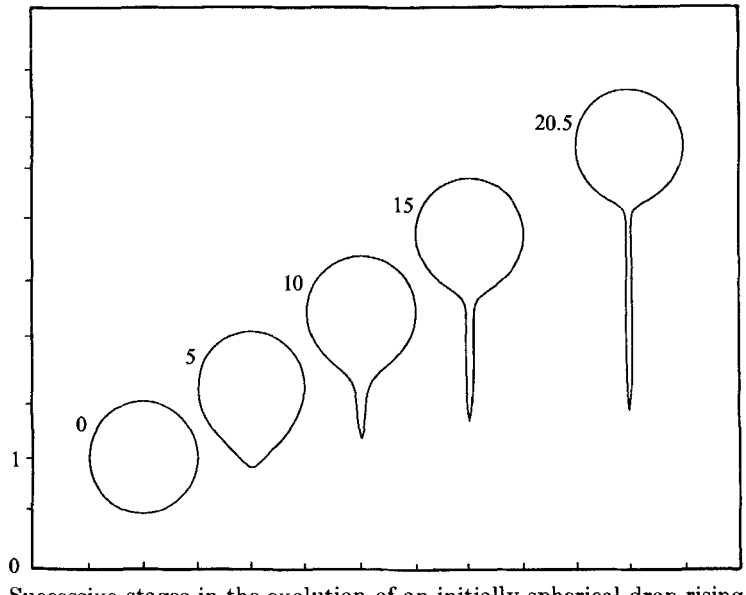

FIGURE 8. Successive stages in the evolution of an initially spherical drop rising away from a plane wall, for $\lambda = 0.10$, $\Gamma = 0$, $\delta = 2.0$. The time is indicated on the left of each frame.

interesting to note that the velocity at the initial instant is independent of Γ. This is a unique feature of the spherical shape. As Γ is increased, the velocity curves shift towards the theoretical limit $\Gamma = \infty$. There is an initial relaxation period whose duration is reduced as Γ increases. At large times, all curves show reasonable agreement with the theoretical curve of Bart.

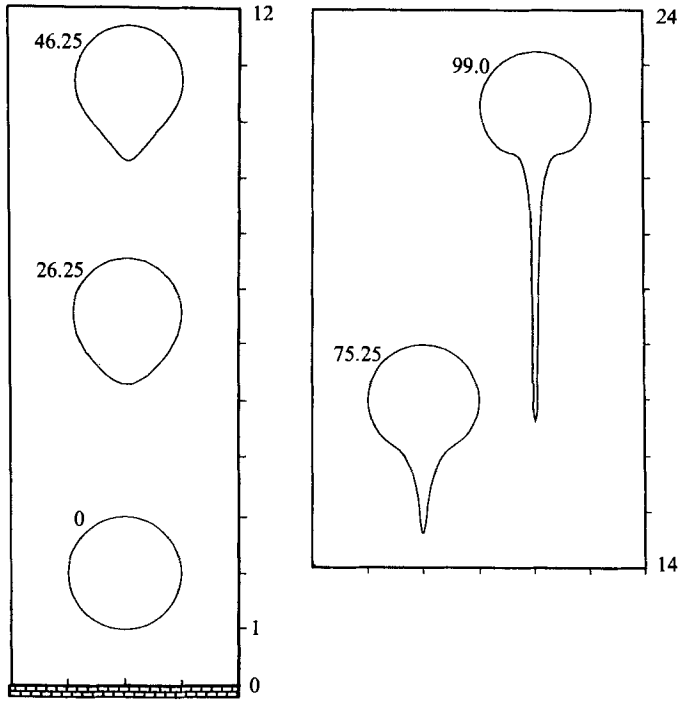

FIGURE 9. Successive stages in the evolution of an initially spherical drop rising away from a plane wall, for $\lambda = 5$, $\Gamma = 0$, $\delta = 2.0$. The time is indicated on the left of each frame.

Next, we examine the effect of the viscosity ratio λ. In figures 8 and 9 we present characteristic stages in the drop evolution for $\lambda = 0.10$ and 5. We observe that decreasing λ makes the drop more flexible, and hence, more susceptible to the deforming action of the wall. Increasing λ causes a proportional increase in the size of the developing tail, a behaviour similar to that of prolate drops moving in an infinite ambient fluid (Pozrikidis 1990). Additional calculations have shown that the effect of surface tension is similar to that for the case $\lambda = 1$, as discussed above.

Figures 8 and 9 indicate that the rate of drop deformation is a strong function of the viscosity ratio λ, and that increasing λ increases the timescale of deformation T. This is consistent with linear analysis for a slightly deformed drop moving in an infinite ambient fluid (Kojima *et al.* 1984) indicating that T is proportional to $a(\lambda+1)/U$, where U is the terminal velocity of the drop. Unfortunately, a similar linear analysis for a drop evolving in the presence of a wall is considerably more involved, preventing the derivation of a simple scaling law (Chervenivanova & Zapryanov 1985). To quantify the dependence of T on λ, we define as an index of the overall drop deformation, the size of the drop in the vertical axial l. In figure 10 we plot l as a function of reduced time $t^* = tU/a(\lambda+1)$ for $\lambda = 0.10$, 1.0, and 5.0. We observe that at small times and up to approximately $t^* = 1$, the three curves lie close to each other, indicating that $(\lambda+1)\,a/U$ is the proper timescale of deformation. This scale becomes invalid at later times. Asymptotically at large times, the rate of deformation becomes proportional to the speed of rise, and the slope of the curves in figure 10 becomes approximately equal to $\lambda+1$.

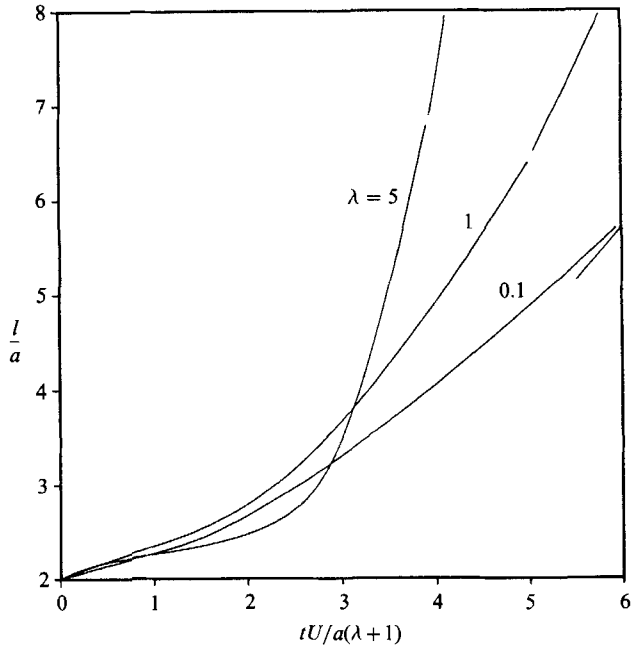

FIGURE 10. The size of the drop in the axial direction as a function of reduced time, for different viscosity ratios. The slope of the straight lines at large times is equal to $\lambda+1$.

3.2. *Drops moving towards the wall*

In the second part of our investigation we consider drops settling towards the wall. We start by considering the deformation of a spherical drop initially located at $\delta = 8$, with $\lambda = 1$ and $\Gamma = 0$, depicted in figure 11(*a*). In the initial stages of the motion, the presence of the wall introduces a disturbance flow which causes the drop to deform into an oblate spheroid ($t = 10$). This initiates a hydrodynamic instability which causes the development of a dimple at the top boundary of the drop ($t = 20$, 30) (Pozrikidis 1990). The bottom part of the drop maintains a nearly spherical shape during this stage of motion. As the drop approaches the wall, it slows down, and starts spreading in the radial direction ($t = 45$). The bottom boundary of the drop flattens out, and a thin layer of ambient fluid is trapped between the drop and the wall. At the same time, the top boundary of the drop levels out under the influence of the flow generated by the radial spreading ($t = 60$). At later times, the bottom boundary of the drop develops an axisymmetric dimple with centre on the axis of motion ($t = 70.5$). At the initial stages of spreading, the thickness of the film trapped beneath the drop decreases in a uniform fashion. As time proceeds, however, fluid in the film moves towards the centre of the dimple causing an increase in the thickness of the film at the centreline, and generating a localized protrusion ($t = 110.5, 238$). We recall now that the film beneath the drop is gravitationally unstable, for it is located below the high-density drop fluid. As a result, it becomes susceptible to gravitational instabilities which tend to amplify the size of the formed protrusion ($t = 313$). The details of this motion may be better understood by considering the instantaneous streamlines shown in figure 11(*b*). The presence of a toroidal eddy attached to the wall is a clear indication of upward fluid motion.

To illustrate the effect of the initial location of the drop on its deformation, in figure 12(*a*) we present three characteristic stages in the evolution of an initially

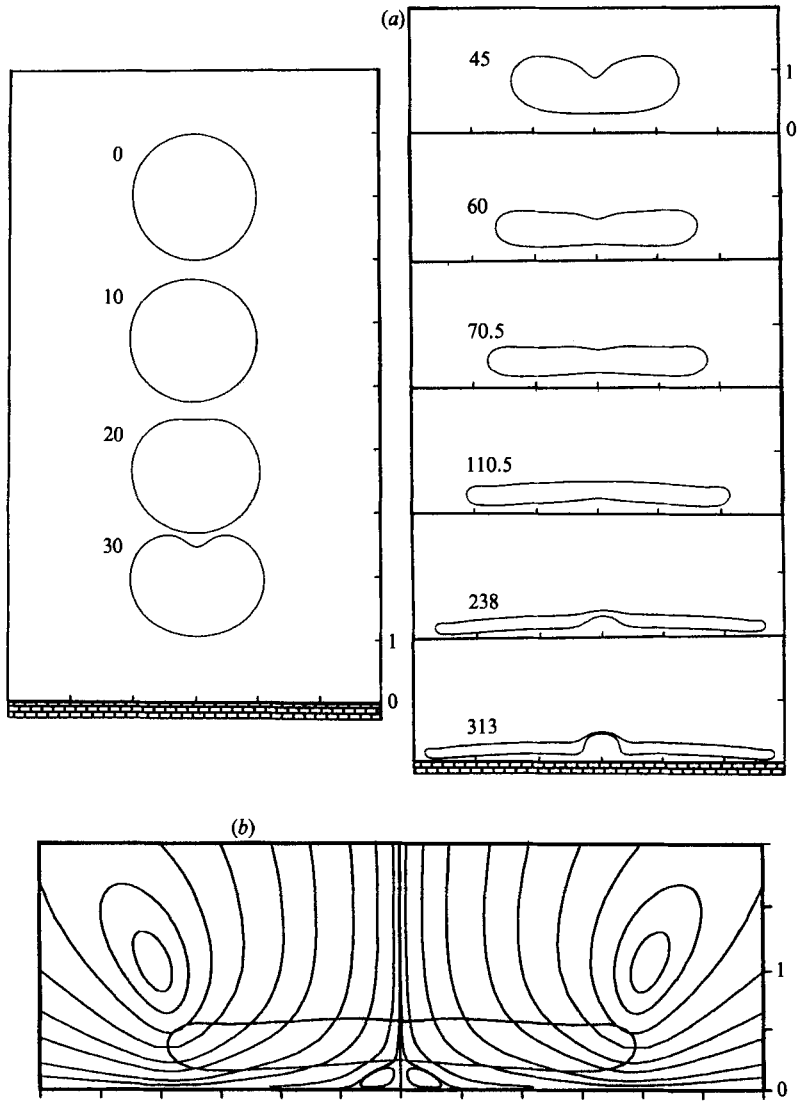

FIGURE 11. (*a*) Successive stages in the evolution of an initially spherical drop falling towards a plane wall from a vertical distance $\delta = 8.0$, for $\lambda = 1$, $\Gamma = 0$. The time is indicated on the left of each frame. (*b*) The instantaneous streamline pattern at $t = 80.5$.

spherical drop released from $\delta = 2$, with $\lambda = 1$, and $\Gamma = 0$. In this case, the top boundary of the drop remains convex throughout the motion. As the drop starts spreading over the wall, a dimple develops at its lower boundary in a process similar to that illustrated in figure 11 (*a*). Comparing figure 12 (*a*), $t = 40$ with figure 11 (*a*), $t = 70.5$, suggests that changing the initial location of the drop produces only subtle variations in the shape of the drop at the initial stages of spreading. Note, however, that the thickness of the drop at the centreline in figure 11 (*a*) is slightly reduced owing to the dimpling of the top boundary of the drop during the early stages of motion. Comparing figure 12 (*a*), $t = 292.5$ with figure 11 (*a*), $t = 313$, suggests that subtle variations in the drop shape may have a profound effect on the future of the thin layer which is trapped beneath the drop. The reason for this behaviour becomes

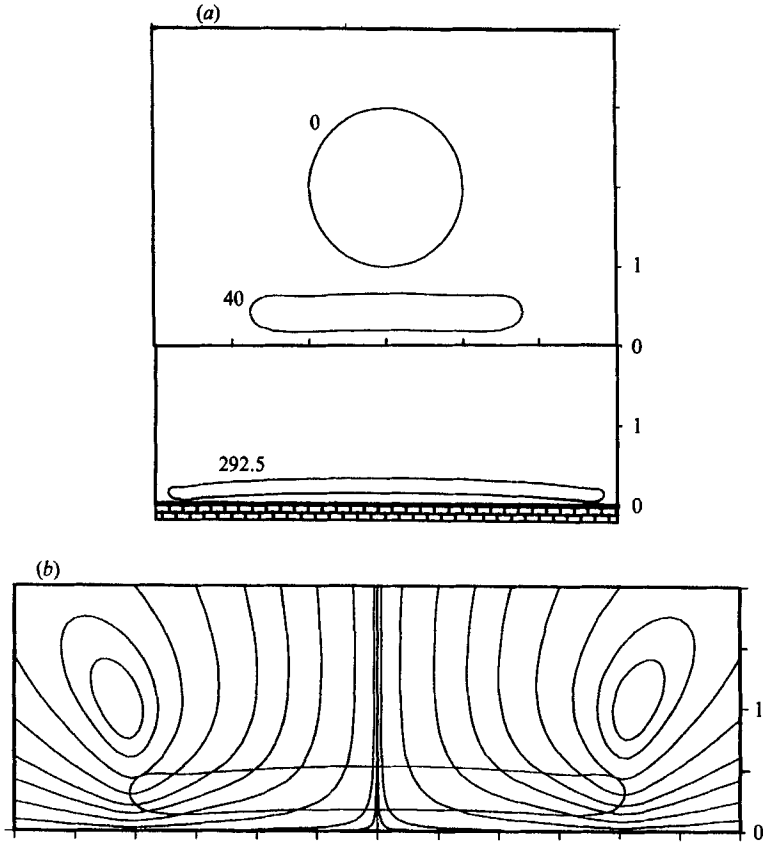

FIGURE 12. (a) Successive stages in the evolution of an initially spherical drop falling towards a plane wall from a vertical distance $\delta = 2.0$, for $\lambda = 1$, $\Gamma = 0$, $\delta = 2.0$. (b) The instantaneous streamline pattern at $t = 70$.

clear by comparing the instantaneous streamline pattern shown in figure 12 (b) with that shown in 11 (b). In the former case, there is no eddy attached to wall, suggesting that the trapped film thins in a uniform manner.

From the above calculations we learn that at the final stages of settling, the drop reduces to a spreading layer of fluid that rests over a second layer of ambient fluid. These two layers deform under the action of the flow induced by the spreading of the drop, and evolve under the influence of gravitational instabilities. Figures 11 and 12 present characteristic examples where one or the other mechanism assumes the dominant role.

To further investigate the effect of the initial drop shape, in figure 13 we present four characteristic stages in the evolution of an initially prolate drop released from $\delta = 8$, with $\epsilon = 0.20$, $\lambda = 1$, and $\Gamma = 0$. The evolution of this drop is quite different from that described in figure 11 (a) for $\epsilon = 0$. In the present case, at the initial stages of motion, the drop develops a trailing tail. Ambient fluid is entrained into the drop right above the base of the tail ($t = 30$). This behaviour is reminiscent of that of prolate drops settling in an infinite fluid, and suggests that at the initial stages of motion, the presence of the wall is of minor dynamical importance (Pozrikidis 1990). As the drop approaches the wall, it slows down, and starts spreading in the radial direction ($t = 55$). The drop fluid that has escaped into the tail starts discharging into

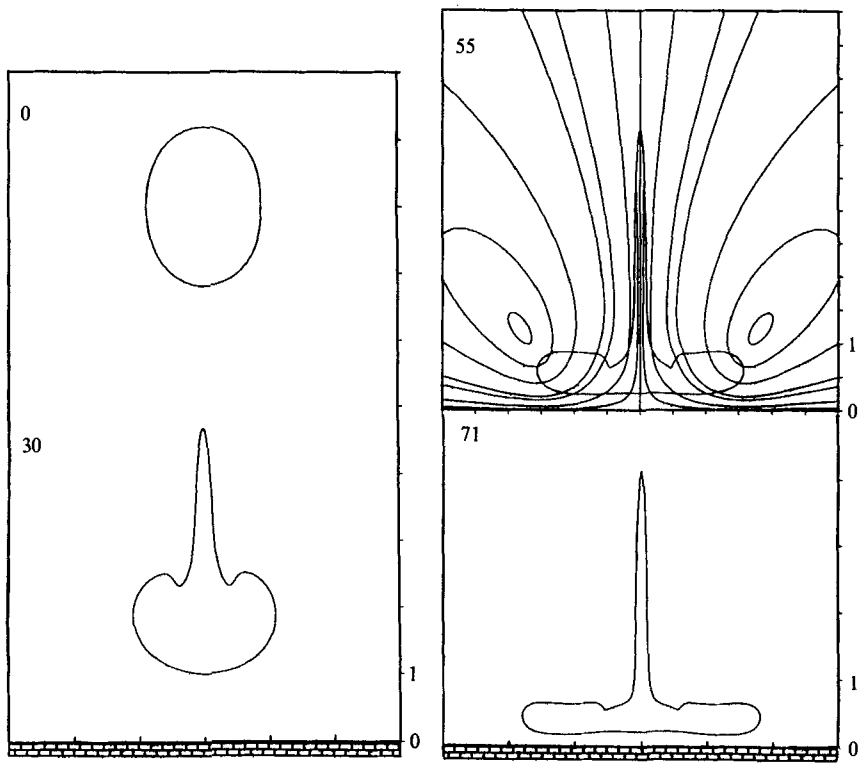

FIGURE 13. Successive stages in the evolution of an initially prolate drop with $\epsilon = 0.20$, falling towards a plane wall from a vertical distance $\delta = 8.0$, for $\lambda = 1$, and $\Gamma = 0$. The time is indicated on the left of each frame.

the main body of the drop, and a two-lobed dimple forms at the bottom boundary of the drop ($t = 71$). The instantaneous streamline pattern shown for $t = 55$ helps us visualize the long-time evolution. Overall, comparing figure 13 to figure 11(*a*) suggests that the initial shape of the drop can play an important role in the general features of deformation.

Next, we consider the effect of the viscosity ratio λ. Thus, in figure 14(*a*, *b*) we present characteristic stages in the evolution of an initially spherical drop released from $\delta = 2$, for $\lambda = 5$ and 0.10. These figures should be viewed in comparison with figure 12, corresponding to $\lambda = 1$. In the case $\lambda = 5$, the top boundary of the drop maintains a nearly spherical-cap shape throughout the evolution (figure 14*a*). This is attributed to its pronounced resistance to deformation owing to its high viscosity. In contrast, in the case $\lambda = 0.10$, the top boundary of the drop becomes locally concave at an early stage of the motion (figure 14*b*). As the viscosity ratio is increased, the thickness of the film trapped underneath the drop is reduced. This is because as the drop becomes more viscous, it requires a longer time for spreading, allowing more time for fluid to escape from underneath. Comparing the times corresponding to the evolution stages of figures 14(*a*, *b*), indicates that increasing the viscosity ratio appreciably reduces the rate of drop deformation.

The instantaneous streamline pattern for the evolution stages shown in figure 14(*a*, *b*) are similar to those shown in figure 12(*b*) for $\lambda = 1$. The velocity profiles, however, present certain interesting variations. Let us focus particular attention on the thin film trapped underneath the drop, and consider radial velocity profiles at

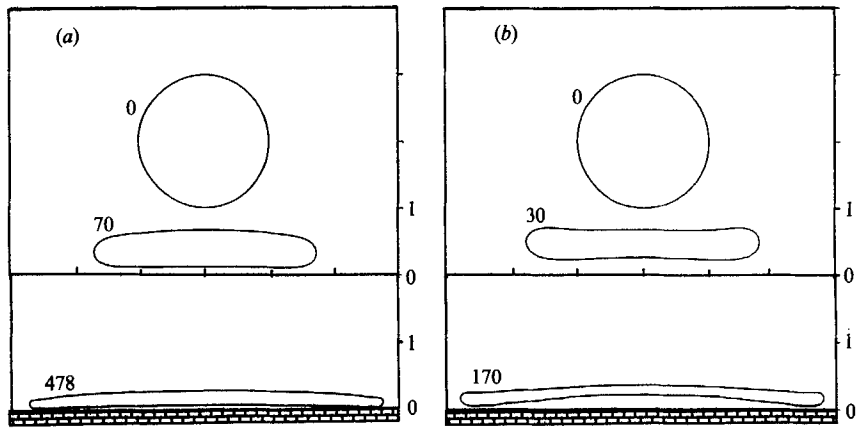

FIGURE 14. Successive stages in the evolution of an initially spherical drop falling towards a plane wall from a vertical distance $\delta = 2.0$, for $\Gamma = 0$, and (a) $\lambda = 5$, (b) $\lambda = 0.10$. The time is indicated on the left of each frame.

different radial locations (figure 15*a*, *b*). For $\lambda = 5$, the velocity profiles are nearly linear within the film, and nearly flat within the drop, figure 15(*a*). For $\lambda = 0.10$, the velocity profiles are nearly parabolic both within the film and the drop (figure 15*b*). In both cases, the slope of the velocity is discontinuous at the surface of the film, so that the shear stress is continuous across the boundary of the drop. Now, because of the slenderness of the shape of the drop at long times, evident in figure 14(*a*, *b*), it appears reasonable to speculate that the long-time deformation of the spreading drop might be described by a lubrication-type theory. Figure 15(*a*, *b*) suggests that the flow within the film and the spreading drop are coupled, and thus they must be taken simultaneously into consideration. This is because both the velocity and slope of the velocity on either side of the surface of the film have finite values. Put differently, the thickness (and thus, the lengthscale) of the flow within the spreading drop is comparable with that within the underlying film, preventing dynamic decoupling.

We now turn to examine the effect of surface tension. Everyday experience suggests that assigning to the drop a finite amount of surface tension will prevent unrestricted spreading. This is confirmed by figure 16(*a*, *b*, *c*), showing three characteristic advanced shapes for $\lambda = 1$, and $\Gamma = 0.10$, 0.50, and 1.0. For all three cases, the drop is initially a sphere with centre at $\delta = 2$. For all three configurations shown in figure 16, the upper boundary of the drop has already attained a nearly steady hydrostatic shape. This becomes evident by considering the capillary pressure force Γk as a function of the gravitational pressure force x, along the drop contour, plotted in figure 17. The fact that over the main body of the drop these pressures vary in a linear manner and with slope equal to minus one, indicates the insignificance of viscous stresses, and suggests negligible fluid motion and boundary deformation. Viscous stresses make significant contributions within the thin layer beneath the drop, and up to the rim of the dimple beneath the drop.

The hydrostatic shape of a drop attached to a wall was described by Bashforth & Adams (1883) as a function of two dimensionless parameters. These include the apparent contact angle ϕ between the drop and the wall, and the parameter $(b/a)^2/\Gamma$, where b is the radius of curvature at the top of the drop, and a is the equivalent radius of the drop. The ratio b/a is a function of ϕ (see Hartland 1967). In our computations, Γ is an independent parameter, whereas ϕ is a dependent parameter whose value is

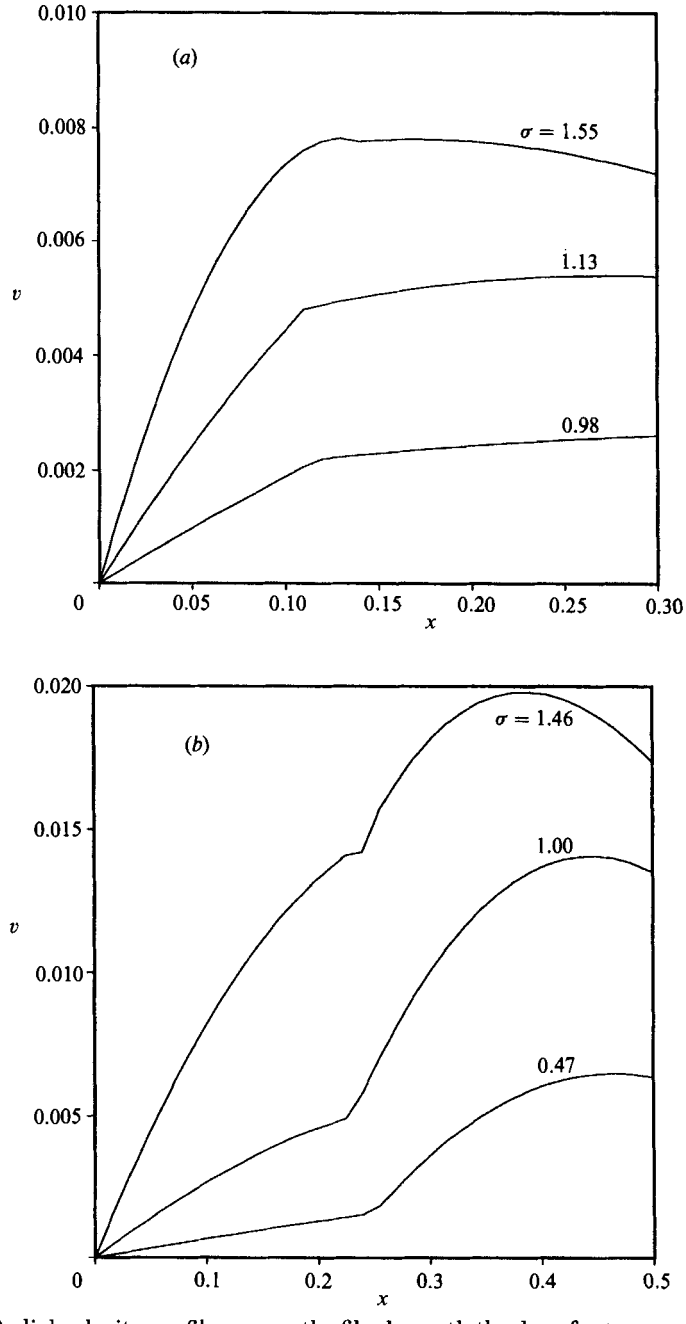

FIGURE 15. Radial velocity profiles across the film beneath the drop for two evolution stages shown in figure 14: (*a*) $\lambda = 5$, $t = 70$, (*b*) $\lambda = 0.10$, $t = 30$. The apparent discontinuities correspond to the boundary of the drop.

determined by the initial drop configuration, and by the viscosity ratio. Figure 16 shows that increasing Γ causes the drop to attain an increasingly more spherical, more compact asymptotic shape. The initial drop configuration and the viscosity ratio λ have little effect on the asymptotic drop shape, and thus on the apparent contact angle ϕ. For instance, computations with $\lambda = 1$, $\Gamma = 0.50$, and $\epsilon = \pm 0.20$,

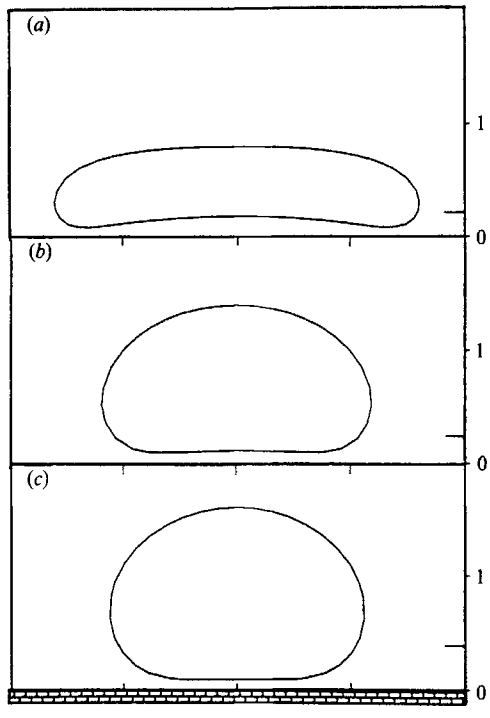

FIGURE 16. Advanced stages in the evolution of an initially spherical drop falling against a plane wall from a vertical distance $\delta = 2.0$, for $\lambda = 1$, and (*a*) $\Gamma = 0.10$, $t = 70$, (*b*) $\Gamma = 0.50$, $t = 28.9$, (*c*) $\Gamma = 1.0$, $t = 21.05$. The drop contour above the indicated horizontal lines has already reached its asymptotic hydrostatic configuration, as shown in figure 17.

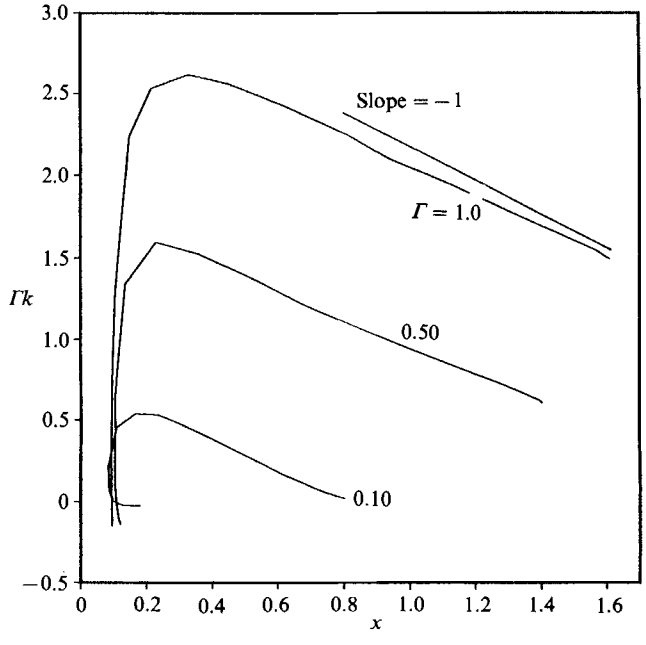

FIGURE 17. The capillary pressure $P_c = \Gamma k$, where k is the curvature of the boundary, as a function of $P_g = x$ along the boundary of the drop, for the three cases depicted in figure 16. A slope of unity indicates a balance between capillary and gravitational forces, and implies negligible fluid motion and boundary deformation.

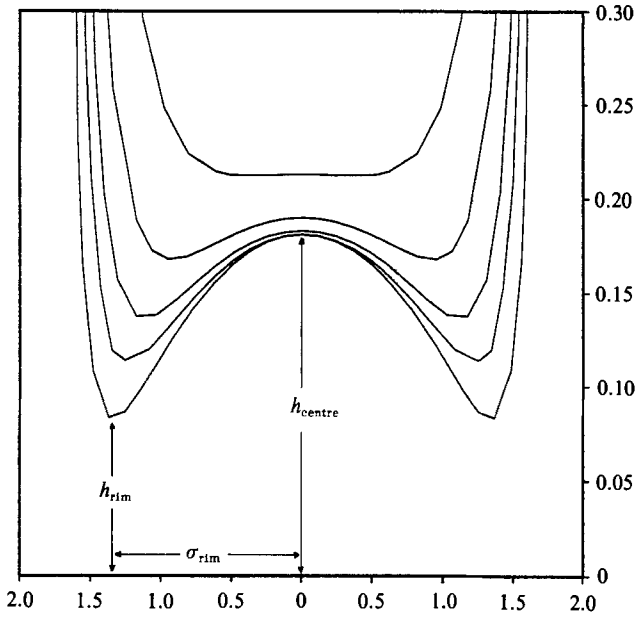

FIGURE 18. The evolution of the dimple beneath the drop for $\lambda = 1$, $\Gamma = 0.10$ (shown in figure 16*a*), on a compressed system of axis. Starting from the top, $t = 20, 30, 40, 50, 70$.

produced asymptotic shapes visually indistinguishable from those shown in figure 16. This behaviour is in agreement with the experimental observations of Hartland (1969).

We saw that in the presence of finite surface tension, the main portion of the drop attains a nearly steady asymptotic configuration, and that the long-time evolution of the drop is due to the deformation of the thin film which is trapped beneath the drop. Thus, the long-time behaviour of this film merits detailed consideration. Examining its evolution, it is helpful to keep in mind that the flow within this film is driven by three mechanisms: the radial pressure field due to capillary forces, the gravitational field due to the discontinuity in density across the surface of the film, and the radial pressure field set up to support the drop. We saw that as a drop approaches the wall, its bottom part flattens, eventually forming an axisymmetric dimple. The evolution of the dimple for $\lambda = 1$, $\Gamma = 0.10$ is illustrated in figure 18 on a compressed system of axes. Crudely speaking, the dimple may be characterized by three geometrical parameters: the radial position of the rim σ_{rim}, the thickness of the trapped film at the rim h_{rim}, and the thickness of the film at the centreline h_{centre}. As soon as the dimple forms, σ_{rim} increases, while h_{rim} decreases in time in a monotonic fashion. h_{centre} initially decreases, goes through a minimum, and then starts increasing, as illustrated in figure 19. This type of behaviour is in agreement with the experimental observations of Hartland (1969) (see in particular figures 3 and 5 corresponding to $\lambda = 1.28$, $\Gamma = 0.34$). Unfortunately, our numerical procedure is not capable of describing the long-time behaviour of the trapped film with sufficient accuracy (the volume of the drop at stages shown in figure 16 has already increased by 2% due to numerical error). Thus, we cannot assert whether h_{centre} will keep increasing, or whether it will reach a maximum, and then start decreasing, as reported by Hartland (1969). A behaviour similar to that shown in figure 18 was also obtained for the cases $\lambda = 1$, and $\Gamma = 0.50, 1.0$. In these cases however, h_{centre}

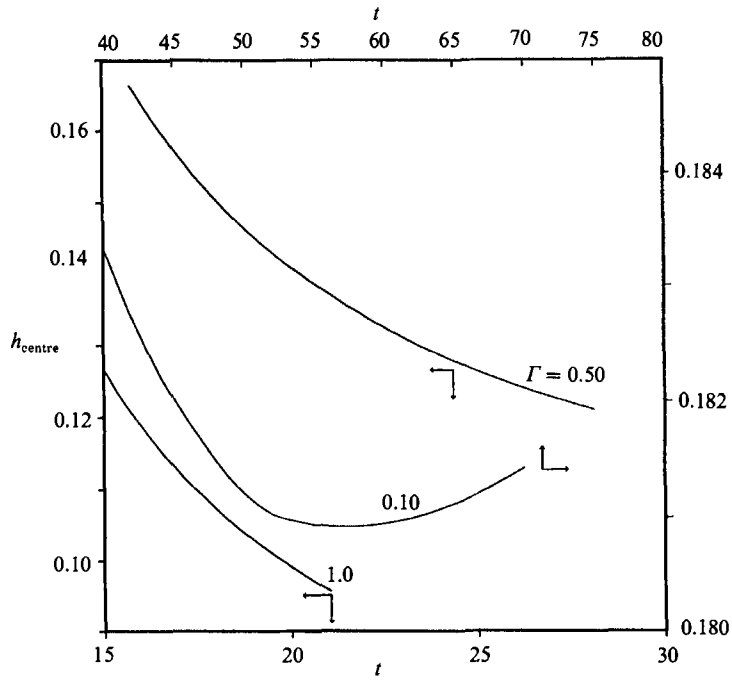

FIGURE 19. The thickness of the film at the centre as a function of time, for the three cases depicted in figure 16.

decreased in a monotonic fashion, as shown in figure 19. The fact that increasing the inverse Bond number causes h_{centre} to decrease in a monotonic fashion is in qualitative agreement with the observations of Hartland (1969).

To gain insight into the structure of the flow within the film, in figure 20(a, b) we present characteristic radial velocity profiles for the drop shapes depicted in figures 16(a, b). The boundary of the film is indicated by vertical bars. Close inspection of figure 20(a) reveals the presence of backflow at $\sigma = 0.11$. This is consistent with the fact that h_{centre} increases at this stage of motion, and indicates the existence of a region of recirculating flow. Indeed, a large region of recirculating flow is evident in the instantaneous streamline pattern shown in figure 21. Turning to figure 20(b), we notice that all profiles appear parabolic to a good approximation.

Now, the slenderness of the film beneath the drop suggests that its evolution might be described by a film-drainage theory. At this point we wish to use our numerical results in order to assess the accuracy of this theory. One central assumption of film-drainage theory is that the pressure gradient across the film is much smaller than that along the film, and thus the flow within the film is essentially unidirectional, and the velocity profile is parabolic. The velocity must vanish along the solid wall, and the shear stress must be continuous across the film surface. The surface-shear stress on the side of the film is of order $\mu_1 v_S/h$, where h is the film thickness. On the other hand, the surface-shear stress on the side of the drop is of order $\mu_2 v_S/c$, where c is a characteristic lengthscale of the fluid motion within the drop, and v_S is the interfacial velocity. For a slightly deformed drop at small Bond numbers, c is of order $(ah)^{\frac{1}{2}}$ (Jones & Wilson 1978; Yiantsios & Davis 1990). The ratio of the shear stress at the film surface to that in the interior of the film is thus proportional to $\lambda h/c$. This is a small number provided that $\lambda < c/h$, suggesting that unless the drop is extremely viscous, the surface-shear stress at the surface of the film can be taken to be equal

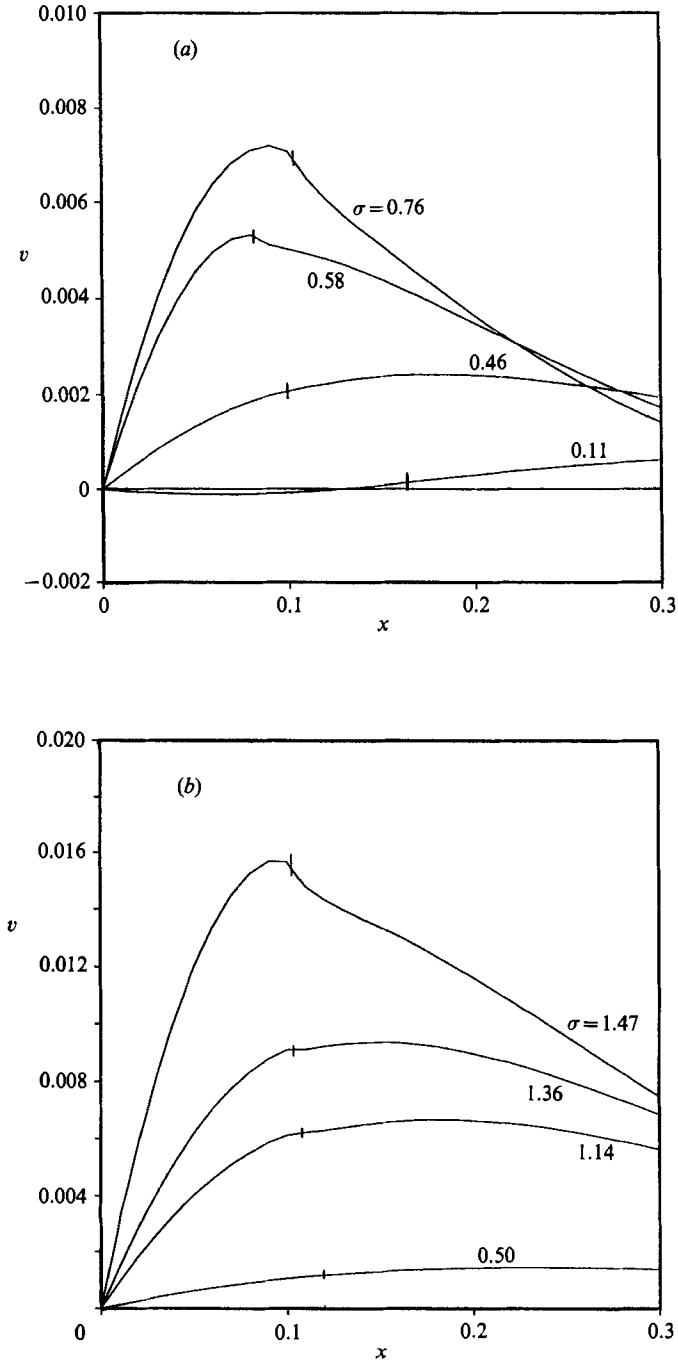

FIGURE 20. Radial velocity profiles across the film beneath the drop for $\lambda = 1$, and (*a*) $\Gamma = 0.10$, at $t = 70$, and (*b*) $\Gamma = 0.50$, at $t = 28.1$. The vertical bars indicate the boundary of the drop.

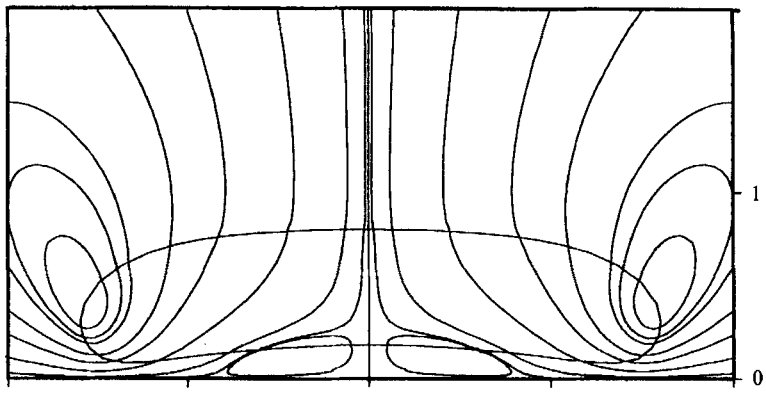

FIGURE 21. Instantaneous streamline pattern at $t = 69.00$ for $\lambda = 1$, $\Gamma = 0.10$.

to zero. This is directly verified by figure 20(*b*), showing that for $\lambda = 1$ and $\Gamma = 0.50$, dv/dx at the film surface is quite small. This, however, is not the case for the case $\lambda = 1$ and $\Gamma = 0.10$, as indicated by figure 20(*a*), for the lengthscale of the flow within the drop c is conspicuously comparable with h. Furthermore, under the assumptions of film-drainage theory, the radial velocity profile within the film is given by

$$v = \frac{1}{2\mu_1}\frac{\partial P}{\partial \sigma}x(x-2h), \tag{3.2}$$

whereas the mean radial velocity is related to the surface velocity by

$$v_m = \int_0^h v\,dx = \tfrac{2}{3}v_S. \tag{3.3}$$

In figure 22 (square symbols) we plot the right-hand side versus the left-hand side of (3.3) at different radial positions along the film surface for the configuration shown in figure 16(*c*). The data fall close to the diagonal line, affirming the accuracy of (3.2).

A second central assumption of the film-drainage theory is that the pressure within the film is related to that outside the film through a pressure-jump condition involving gravity and surface tension (although gravity is often ignored). The pressure variation within the drop is assumed to be negligible compared with that within the film. Stated differently, the drop is viewed as a chamber of constant pressure. The pressure within the film is then given by

$$P_{\text{Film}} = P_{\text{Drop}} - \Gamma k - x. \tag{3.4}$$

Substituting this equation into (3.2), and evaluating the resulting equation at the film surface, we obtain

$$v_S = \frac{h^2}{2\mu_1}\left(\Gamma\frac{\partial k}{\partial \sigma} + \frac{\partial h}{\partial \sigma}\right). \tag{3.5}$$

In figure 22 (solid symbols) we plot v_S predicted by (3.5), denoted by v_S^{FD}, versus the actual surface velocity computed in our numerical procedure for the configuration shown in figure 16(*c*). Within the film region, the data fall reasonably close to the diagonal line suggesting that the conditions of the film-drainage theory are met. Similar results pertain to the case $\lambda = 1$ and $\Gamma = 0.50$, shown in figure 20(*b*). Of course, closure of the film-drainage theory requires a boundary condition for the shape of the drop beyond the rim of the dimple. Implementation of this condition

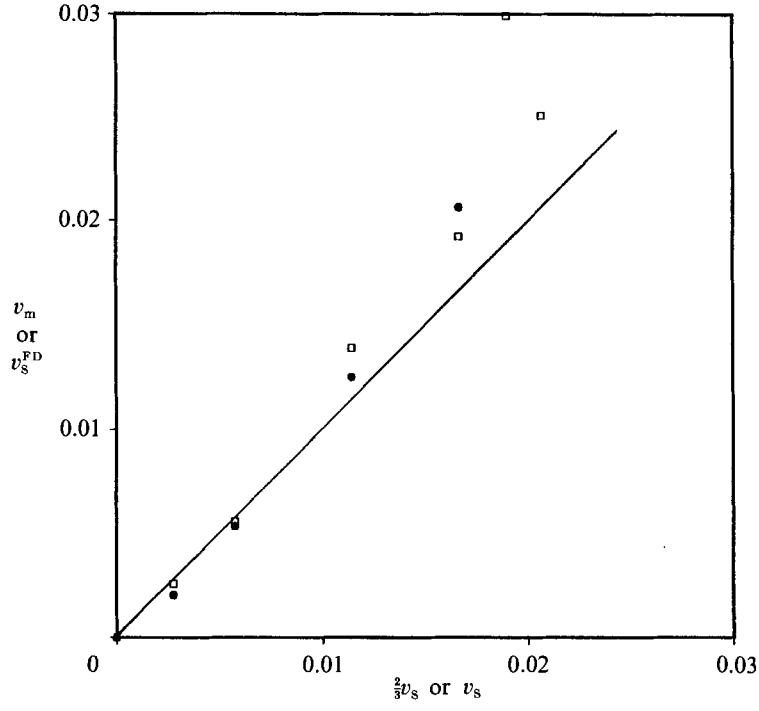

FIGURE 22. The mean-film velocity (square symbols), and the surface velocity predicted by film-drainage theory (solid symbols), plotted versus the actual velocity at the film surface, for $\lambda = 1$, $\Gamma = 1.0$ (see figure 16*c*).

presumes knowledge of the corresponding hydrostatic drop shape, and this must be found through numerical solutions as previously discussed.

We saw that all of the assumptions used by the film-drainage theory are met for the configurations shown in figure 16(*b*, *c*). Unfortunately, the inverse Bond number Γ corresponding to these configurations is not large enough for the asymptotic version of this theory at large Γ to be valid (Hartland 1969; Hartland & Robinson 1977; Jones & Wilson 1978; Lin & Slattery 1982; Wu & Weinbaum 1982; Williams & Davis 1982; Yiantsios & Davis 1990). This may be clearly seen by noting that film-drainage theory predicts that at high values of Γ the radius of the rim is given by $\sigma_{\rm rim} = (\frac{2}{3}\Gamma)^{\frac{1}{2}}$. For $\Gamma = 0.50$ and 1.0 this predicts $\sigma_{\rm rim} = 1.15$ and 0.82 which are in marked disagreement with the shapes shown in figure 16(*b*, *c*). Unfortunately, calculations at high Γ were prohibited by difficulties in the numerical procedure as discussed in §2.

4. Summary

We performed a numerical study of the deformation of a viscous drop moving normal to a plane wall. We found that when the drop is far away from the wall, its evolution is similar to that of an isolated drop moving in an infinite fluid. Depending on its initial position and shape, as well as on surface tension, a rising drop may deform into a variety of shapes. The theory of non-deforming drops provides an accurate estimate for the speed of rise. In the absence of surface tension, a drop falling towards a wall keeps spreading in the radial direction, eventually reducing to a thin layer of fluid. The bottom of the drop develops a dimple during the late stages

of settling. Surface tension restricts spreading, and forces to drop to attain a steady configuration. A thinning film of ambient fluid is trapped between the drop and the wall whose evolution may follow a variety of protocols. These are in qualitative agreement with experimental observations. We were not able to compute the long-time behaviour of the trapped film with sufficient accuracy. We were able to affirm, however, that when surface tension is sufficiently large, the evolution of the film may be accurately described using the film-drainage theory.

Simultaneously with the present work, Ascoli *et al.* (1990) performed a numerical study of the motion of a viscous drop settling towards a plane solid wall. Certain important differences between the present work and that of Ascoli *et al.*, regarding the problem formulation and numerical method of solution, were indicated in §2. Overall, the conclusions of Ascoli *et al.* are in general agreement with those of the present paper.

Thanks are due to the office of academic computing of UCSD and to the NSF for providing computational resources with the SDSC. Acknowledgement is made to the donors of The Petroleum Research Fund, administered by the ACS, for partial support of this research. This work is partially supported by the National Science Foundation, Program of Fluid Dynamics and Hydraulics, Grant MSM 88-20350.

Appendix A

When the domain of a flow is bounded internally or externally by a solid boundary S_B, it is convenient to use a Green function whose induced velocity vanishes on S_B

$$G_{ij}(\boldsymbol{x}, \boldsymbol{x}_0) = 0 \quad \text{when } \boldsymbol{x} \text{ lies on } S_B. \tag{A 1}$$

Examples of such known Green functions include those for flow bounded by a solid plane wall (Blake 1971), a semi-infinite plane wall (Hasimoto, Kim & Miyazaki 1983), a solid sphere (Oseen 1927, p. 108), two intersecting planes (Sano & Hasimoto 1978), an infinite circular cylinder (Liron & Shahar 1978), and a solid plane wall with a circular hole (Miyazaki & Hasimoto 1984). We shall show that all of these Green functions satisfy the symmetry property

$$G_{ij}(\boldsymbol{x}, \boldsymbol{x}_0) = G_{ji}(\boldsymbol{x}_0, \boldsymbol{x}). \tag{A 2}$$

For this purpose, we consider the flow induced by the translation of a solid particle in the presence of the surface S_B, and write the boundary integral equation

$$u_j(\boldsymbol{x}_0) = -\frac{1}{8\pi\mu} \int_{S_P, S_B} [f_i G_{ij}(\boldsymbol{x}, \boldsymbol{x}_0) - \mu u_i T_{ijk}(\boldsymbol{x}, \boldsymbol{x}_0) \hat{n}_k] \, dS, \tag{A 3}$$

where S_P is the surface of the particle. On S_P, $\boldsymbol{u}$ is a constant equal to $\boldsymbol{U}$. Exploiting the fact that both $\boldsymbol{u}$ and $\boldsymbol{G}(\boldsymbol{x}, \boldsymbol{x}_0)$ vanish when $\boldsymbol{x}$ lies on S_B, and using the identity

$$\int_{S_P} T_{ijk}(\boldsymbol{x}, \boldsymbol{x}_0) \hat{n}_k \, dS = 0, \tag{A 4}$$

valid for a point $\boldsymbol{x}_0$ which is located outside S_P, we reduce (A 3) to

$$u_j(\boldsymbol{x}_0) = -\frac{1}{8\pi\mu} \int_{S_P} f_i G_{ij}(\boldsymbol{x}, \boldsymbol{x}_0) \, dS. \tag{A 5}$$

This equation is valid within the domain of the flow, as well as on the boundaries of the flow S_B, and S_P. Alternatively, we represent the flow via a single-layer potential of the type

$$u_j(\boldsymbol{x}_0) = \frac{1}{8\pi\mu}\int_{S_P} G_{ji}(\boldsymbol{x}_0, \boldsymbol{x})\, q_i \, \mathrm{d}S, \tag{A 6}$$

where $\boldsymbol{q}$ is the density of the distribution. The stress field associated with this distribution is given by

$$\sigma_{ik}(\boldsymbol{x}_0) = \frac{1}{8\pi}\int_{S_P} T_{ijk}(\boldsymbol{x}_0, \boldsymbol{x})\, q_j \, \mathrm{d}S, \tag{A 7}$$

and the surface stress on either side of the surface of the particle is equal to

$$(f_i)^{\pm}(\boldsymbol{x}_0) = -\frac{\pm 1}{2} q_i(\boldsymbol{x}_0) + \frac{1}{8\pi}\hat{n}_k(\boldsymbol{x}_0)\int_{S_P}^{\mathrm{PVI}} T_{ijk}(\boldsymbol{x}_0, \boldsymbol{x})\, q_j \, \mathrm{d}S, \tag{A 8}$$

where the plus sign corresponds to the external side, and the minus sign to the internal side. Recalling that on S_P the velocity satisfies the boundary condition $\boldsymbol{u} = \boldsymbol{U}$, suggests that the interior of the particle $(f_i)^- = P\hat{n}_i$ where P is the constant internal pressure. Equation (A 8) then gives

$$(\boldsymbol{f})^+ = P\hat{\boldsymbol{n}} - \boldsymbol{q}. \tag{A 9}$$

Substituting (A 9) into (A 5), and using the identity

$$\int_{S_P} G_{ij}(\boldsymbol{x}, \boldsymbol{x}_0)\, \hat{n}_j \, \mathrm{d}S = 0,$$

a direct consequence of the continuity equation, we obtain

$$u_j(\boldsymbol{x}_0) = \frac{1}{8\pi\mu}\int_{S_P} q_i \, G_{ij}(\boldsymbol{x}, \boldsymbol{x}_0)\, \mathrm{d}S. \tag{A 10}$$

Subtracting (A 10) from (A 6) produces (A 2). An alternative method for proving (A 2) is presented by Jaswon & Symm (1977, p. 80).

We now proceed to show that the pressure vector $\boldsymbol{p}$ and the stress tensor $\boldsymbol{T}$ corresponding to the above Green functions, constitute legitimate solutions to the equations of creeping motion. Specifically, we shall show that

$$u_j(\boldsymbol{x}_0) = p_j(\boldsymbol{x}, \boldsymbol{x}_0)\, \beta \tag{A 11}$$

and

$$u_j(\boldsymbol{x}_0) = T_{ijk}(\boldsymbol{x}, \boldsymbol{x}_0)\, g_{ik}, \tag{A 12}$$

where β and $\boldsymbol{g}$ are arbitrary constants, represent acceptable Stokes velocity fields. For this purpose, we write the boundary integral equation for flow in a domain bounded by an arbitrary surface D and also by S_B. With the aid of (A 2) this takes the form

$$u_j(\boldsymbol{x}_0) = -\frac{1}{8\pi\mu}\int_D [G_{ji}(\boldsymbol{x}_0, \boldsymbol{x}) f_i - \mu u_i \, T_{ijk}(\boldsymbol{x}, \boldsymbol{x}_0)\, \hat{n}_k] \, \mathrm{d}S. \tag{A 13}$$

The first part of the integral on the right-hand side represents the flow due to a distribution of Green functions, with density distribution $\boldsymbol{f}$. The second term represents the flow due to a double-layer potential with density $\boldsymbol{u}$. The fact that $\boldsymbol{u}$ can be specified on D in an arbitrary manner, implies that the flow (A 12) satisfies the

equations of creeping motion. Invoking now the definition of $\boldsymbol{T}$, and using (A 2), we write

$$T_{ijk}(\boldsymbol{x},\boldsymbol{x}_0) = -p_j(\boldsymbol{x},\boldsymbol{x}_0)\,\delta_{ik} + \frac{\partial G_{ji}(\boldsymbol{x}_0,\boldsymbol{x})}{\partial x_k} + \frac{\partial G_{jk}(\boldsymbol{x}_0,\boldsymbol{x})}{\partial x_i}. \tag{A 14}$$

The differential terms represent derivative singularities and, hence, they constitute acceptable solutions to the equations of creeping flow. Thus, the pressure term and hence (A 11), must be a legitimate singular solution to the equations of creeping flow as well. In particular, the velocity field (A 11) expresses the flow produced by a point source of strength $-8\pi\beta$ in the presence of the bounding solid surface S_{B}.

Appendix B

We give here the defining expressions for the various matrices introduced in the main body of the paper. The matrix $\boldsymbol{M}$ is defined as

$$\boldsymbol{M}(\boldsymbol{x},\boldsymbol{x}_0) = \boldsymbol{M}^{\mathrm{ST}}(\boldsymbol{x},\boldsymbol{x}_0) - \boldsymbol{M}^{\mathrm{ST}}(\boldsymbol{x},\boldsymbol{x}_0^{\mathrm{IM}}) + 2h^2\boldsymbol{M}^{\mathrm{D}}(\boldsymbol{x},\boldsymbol{x}_0^{\mathrm{IM}}) - 2h\boldsymbol{M}^{\mathrm{SD}}(\boldsymbol{x},\boldsymbol{x}_0^{\mathrm{IM}}),$$

where
$$M_{11}^{\mathrm{ST}} = \sigma(I_{10}+\hat{x}^2 I_{30}),\quad M_{11}^{\mathrm{D}} = \sigma(-I_{30}+3\hat{x}^2 I_{50}),\quad M_{11}^{\mathrm{SD}} = \hat{x}M_{11}^{\mathrm{SD}},$$
$$M_{12}^{\mathrm{ST}} = \sigma\hat{x}(\sigma I_{30}-\sigma_0 I_{31}),\quad M_{12}^{\mathrm{D}} = \sigma 3\hat{x}(\sigma I_{50}-\sigma_0 I_{51}),\quad M_{12}^{\mathrm{SD}} = \hat{x}M_{12}^{\mathrm{D}} - \sigma(\sigma I_{30}-\sigma_0 I_{31}),$$
$$M_{21}^{\mathrm{ST}} = \sigma\hat{x}(\sigma I_{31}-\sigma_0 I_{30}),\quad M_{21}^{\mathrm{D}} = -3\sigma\hat{x}(\sigma I_{51}-\sigma_0 I_{50}),\quad M_{21}^{\mathrm{SD}} = \hat{x}M_{21}^{\mathrm{D}} - \sigma(\sigma I_{31}-\sigma_0 I_{30}),$$
$$M_{22}^{\mathrm{ST}} = \sigma[I_{11}+(\sigma^2+\sigma_0^2)I_{31}-\sigma\sigma_0(I_{30}+I_{32})],$$
$$M_{22}^{\mathrm{D}} = \sigma[I_{31}-3(\sigma^2+\sigma_0^2)I_{51}+3\sigma\sigma_0(I_{50}+I_{52})],\quad M_{22}^{\mathrm{D}} = \hat{x}M_{22}^{\mathrm{D}},$$

where $\hat{x} = x - x_0$.

The matrix $\boldsymbol{q}$ is defined as

$$\boldsymbol{q}(\boldsymbol{x},\boldsymbol{x}_0) = \boldsymbol{q}^{\mathrm{ST}}(\boldsymbol{x},\boldsymbol{x}_0) - \boldsymbol{q}^{\mathrm{ST}}(\boldsymbol{x},\boldsymbol{x}_0^{\mathrm{IM}}) + 2h^2\boldsymbol{q}^{\mathrm{D}}(\boldsymbol{x},\boldsymbol{x}_0^{\mathrm{IM}}) - 2h\boldsymbol{q}^{\mathrm{SD}}(\boldsymbol{x},\boldsymbol{x}_0^{\mathrm{IM}}),$$

where
$$q_{111}^{\mathrm{ST}} = -6\sigma\hat{x}^3 I_{50},\quad q_{111}^{\mathrm{D}} = -6\sigma\hat{x}(-3I_{50}+5\hat{x}^2 I_{70}),\quad q_{111}^{\mathrm{SD}} = \hat{x}q_{111}^{D},$$
$$q_{112}^{\mathrm{ST}} = q_{121}^{\mathrm{ST}} = -6\sigma\hat{x}^2(\sigma I_{50}-\sigma_0 I_{51}),$$
$$q_{112}^{\mathrm{D}} = q_{121}^{\mathrm{D}} = 6\sigma[\sigma I_{50}-\sigma_0 I_{51}-5\hat{x}^2(\sigma I_{70}-\sigma_0 I_{71})],$$
$$q_{112}^{\mathrm{SD}} = q_{121}^{\mathrm{SD}} = \hat{x}q_{112}^{\mathrm{D}} + 6\sigma\hat{x}(\sigma I_{50}-\sigma_0 I_{51}),$$
$$q_{211}^{\mathrm{ST}} = -6\sigma\hat{x}^2(\sigma I_{51}-\sigma_0 I_{50}),$$
$$q_{211}^{\mathrm{D}} = 6\sigma[-\sigma I_{51}+\sigma_0 I_{50}+5\hat{x}^2(\sigma I_{71}-\sigma_0 I_{70})],$$
$$q_{211}^{\mathrm{SD}} = q_{211}^{\mathrm{SD}} = \hat{x}q_{211}^{\mathrm{D}} + 6\sigma\hat{x}(\sigma I_{51}-\sigma_0 I_{50}),$$
$$q_{122}^{\mathrm{ST}} = -6\sigma\hat{x}(\sigma_0^2 I_{52}+\sigma^2 I_{50}-2\sigma\sigma_0 I_{51}),$$
$$q_{122}^{\mathrm{D}} = 6\sigma\hat{x}[I_{50}-5(\sigma^2 I_{70}-2\sigma\sigma_0 I_{71}+\sigma_0^2 I_{72})],$$
$$q_{122}^{\mathrm{SD}} = \hat{x}q_{122}^{\mathrm{D}} - 6\sigma(\hat{x}^2 I_{50}-\sigma^2 I_{50}-\sigma_0^2 I_{52}+2\sigma\sigma_0 I_{51}),$$
$$q_{221}^{\mathrm{ST}} = q_{212}^{\mathrm{ST}} = -6\sigma\hat{x}[(\sigma^2+\sigma_0^2)I_{51}-\sigma\sigma_0(I_{50}+I_{52})],$$
$$q_{221}^{\mathrm{D}} = q_{212}^{\mathrm{D}} = 6\sigma\hat{x}[-I_{51}+5(\sigma^2+\sigma_0^2)I_{71}-5\sigma\sigma_0(I_{70}+I_{72})],$$
$$q_{221}^{\mathrm{SD}} = q_{212}^{\mathrm{SD}} = \hat{x}q_{221}^{\mathrm{D}},$$
$$q_{222}^{\mathrm{ST}} = -6\sigma[\sigma^3 I_{51}-\sigma_0^3 I_{52}-\sigma^2\sigma_0(I_{50}+2I_{52})+\sigma\sigma_0^2(I_{53}+2I_{51})],$$

$$q^{\mathrm{D}}_{222} = 6\sigma[-3\sigma I_{51}+\sigma_0(I_{50}+2I_{52})+5\sigma\sigma_0^2 I_{73}+5\sigma(\sigma^2+2\sigma_0^2)I_{71}$$
$$-5\sigma_0(2\sigma^2+\sigma_0^2)I_{72}-5\sigma^2\sigma_0 I_{70}],$$
$$q^{\mathrm{SD}}_{222} = \hat{x}q^{\mathrm{D}}_{222}+6\sigma\hat{x}(\sigma I_{51}-\sigma_0 I_{50}).$$

The matrix $\boldsymbol{p}$ is defined as

$$p_{11} = q^{\mathrm{ST}}_{211}, \quad p_{12} = q^{\mathrm{ST}}_{212},$$
$$p_{21} = -6\sigma\hat{x}(\sigma^2 I_{52}+\sigma_0^2 I_{50}-2\sigma\sigma_0 I_{51}),$$
$$p_{22} = -6\sigma(\sigma^3 I_{52}-\sigma_0^3 I_{51}-\sigma^2\sigma_0(I_{53}+2I_{51})+\sigma\sigma_0^2(I_{50}+2I_{52})).$$

In all of the above

$$I_{mn} = \int_0^{2\pi}\frac{\cos^n\varphi}{r^m}\mathrm{d}\varphi = \frac{1}{[\hat{x}^2+(\sigma+\sigma_0)^2]^{m/2}}\int_0^{\frac{\pi}{2}}\frac{(2\cos^2\omega-1)^n}{(1-k^2\cos^2\omega)^{m/2}}\mathrm{d}\omega,$$

where
$$k^2 = \frac{4\sigma\sigma_0}{\hat{x}^2+(\sigma+\sigma_0)^2}.$$

The last integrals may be expressed with the aid of standard tables in terms of complete elliptic integrals of the first and second kind (Gradshteyn & Ryshik 1980, §2.58).

Appendix C

The vertical velocity U of a spherical drop moving normal to a solid wall may be readily extracted from the work of Bart (1968). A slight modification of his equation (24) yields

$$U = 2/9k,$$

where
$$k = \tfrac{4}{3}\sinh\alpha\sum_{n=1}^{\infty}\frac{n(n+1)}{(2n-1)(2n+3)}\left[\frac{\lambda Y_n+2Z_n}{\lambda V_n+T_n}-1\right],$$

with
$$Y_n = 2\sinh(2n+1)\alpha+(2n+1)\sinh 2\alpha,$$
$$Z_n = \cosh(2n+1)\alpha+\cosh 2\alpha,$$
$$V_n = 2\sinh(2n+1)\alpha-(2n+1)\sinh 2\alpha,$$
$$T_n = 4\sinh^2(2n+\tfrac{1}{2})\alpha-(2n+1)^2\sinh^2\alpha,$$

where $\alpha = \cosh^{-1}(\delta)$, and λ is the viscosity ratio. All variables are non-dimensionalized as in the main body of the paper.

REFERENCES

Ascoli, E. P., Dandy, D. S. & Leal, L. G. 1990 Buoyancy-driven motion of a deformable drop toward a plane wall at low Reynolds number. *J. Fluid Mech.* **213**, 287–311.

Bart, E. 1968 The slow unsteady settling of a fluid sphere toward a flat fluid interface. *Chem. Engng Sci.* **23**, 193–210.

Bashforth, F. & Adams, J. C. 1883 *An Attempt to Test the Theories of Capillary Action.* Cambridge University Press.

Batchelor, G. K. 1967 *An Introduction to Fluid Dynamics.* Cambridge University Press.

Blake, J. R. 1971 A note on the image system for a Stokeslet in a no-slip boundary. *Proc. Camb. Phil. Soc.* **70**, 303–310.

CHEN, J.-D. 1984 Effects of London–van der Waals and electric double layer forces on the thinning of a dimpled film between a small drop or bubble and a horizontal solid plane. *J. Colloid Interface Sci.* **98**, 329–341.

CHERVENIVANOVA, E. & ZAPRYANOV, Z. 1985 On the deformation of two droplets in a quasi-steady Stokes flow. *Intl J. Multiphase Flow* **11**, 721–738.

CHERVENIVANOVA, E. & ZAPRYANOV, Z. 1987 On the deformation of a fluid particle moving radially inside a spherical container. *PhysichoChemical Hydr.* **8**, 293–305.

CHI, B. K. & LEAL, L. G. 1989 A theoretical study of the motion of a viscous drop toward a fluid interface at low Reynolds number. *J. Fluid Mech.* **201**, 123–146.

CLIFT, R., GRACE, J. R. & WEBER, M. E. 1978 *Bubbles, Drops, and Particles.* Academic Press.

DIMITROV, D. S. & IVANOV, I. B. 1978 Hydrodynamics of thin liquid films. On the rate of thinning of microscopic films with deformable interfaces. *J. Colloid Interface Sci.* **64**, 97–106.

GRADSHTEYN, I. S. & RYSHIK, I. M. 1980 *Table of Integrals, Series, and Products.* Academic.

HAPPEL, J. & BRENNER, H. 1986 *Low Reynolds Number Hydrodynamics.* Martinus Nijhoff.

HARTLAND, S. 1967 The approach of a liquid drop to a flat plate. *Chem. Engng Sci.* **22**, 1675–1687.

HARTLAND, S. 1969 The profile of the draining film beneath a liquid drop approaching a plane interface. In *Unusual Methods of Separation.* Chem. Engng Prog. Symp. Series vol. 65, pp. 82–89.

HARTLAND, S. & ROBINSON, J. D. 1977 A model for an axisymmetric dimpled draining film. *J. Colloid Interface Sci.* **60**, 72–81.

HASIMOTO, H., KIM, M.-U. & MIYAZAKI, T. 1983 The effect of a semi-infinite plane on the motion of a small particle in a viscous fluid. *J. Phys. Soc. Japan* **52**, 1996–2003.

JASWON, M. A. & SYMM, G. T. 1977 *Integral Equation Methods in Potential Theory and Elastostatics.* Academic.

JONES, A. F. & WILSON, S. D. R. 1978 The film drainage problem in droplet coalescence. *J. Fluid Mech.* **87**, 263–288.

KOJIMA, M., HINCH, E. J. & ACRIVOS, A. 1984 The formation and expansion of a toroidal drop moving in a viscous fluid. *Phys. Fluids* **27**, 19–32.

KOH, C. J. & LEAL, L. G. 1989 The stability of drop shapes for translations at zero Reynolds number through a quiescent fluid. *Phys. Fluids* A **1**, 1309–1313.

LIN, C.-Y. & SLATTERY, J. C. 1982 Thinning of a liquid film as a small drop or bubble approaches a solid plane. *AIChE J.* **28**, 147–156.

LIRON, N. & BLAKE, J. R. 1981 Existence of viscous eddies near boundaries. *J. Fluid Mech.* **107**, 109–129.

LIRON, N. & SHAHAR, R. 1978 Stokes flow due to a Stokeslet in a pipe. *J. Fluid Mech.* **86**, 727–744.

MIYAZAKI, T. & HASIMOTO, H. 1984 The motion of a small sphere in fluid near a circular hole in a plane wall. *J. Fluid Mech.* **145**, 201–221.

OSEEN, C. W. 1927 *Hydrodynamik.* Leipzig.

POZRIKIDIS, C. 1990 The instability of a moving viscous drop. *J. Fluid Mech.* **210**, 1–21.

RALLISON, J. M. 1984 The deformation of small viscous drops and bubbles in shear flows. *Ann. Rev. Fluid Mech.* **16**, 45–66.

RALLISON, J. M. & ACRIVOS, A. 1978 A numerical study of the deformation and burst of a viscous drop in an extensional flow. *J. Fluid Mech.* **89**, 191–200.

SANO, O. & HASIMOTO, H. 1978 The effect of two plane walls on the motion of a small sphere in a viscous fluid. *J. Fluid Mech.* **87**, 673–694.

STONE, H. A. & LEAL, L. G. 1989 Relaxation and breakup of an initially extended drop in an otherwise quiescent fluid. *J. Fluid Mech.* **198**, 399–427.

TRAN-CONG, T. & PHAN-THIEN, N. 1989 Stokes problems of multiparticle systems. A numerical method for arbitrary flows. *Phys. Fluids* A **1**, 453–461.

WHITEHEAD, J. A. 1988 Fluid models of geological hotspots. *Ann. Rev. Fluid Mech.* **20**, 61–87.

WILLIAMS, M. B. & DAVIS, S. H. 1982 Nonlinear theory of film rupture. *J. Colloid Interface Sci.* **90**, 220–228.

WU, R. & WEINBAUM, S. 1982 On the development of fluid trapping beneath deformable fluid-cell membranes. *J. Fluid Mech.* **121**, 315–343.

YIANTSIOS, S. G. & DAVIS, R. H. 1990 On the buoyancy driven motion of a drop towards a rigid surface or a deformable interface. *J. Fluid Mech.* (Submitted).